Archive of Applied Mechanics (2025) 95:116
https://doi.org/10.1007/s00419-025-02832-5

ORIGINAL

**Erdal Öner · Mine Gül Oktay · Ecren Uzun Yaylacı · Murat Yaylacı · İrem Mirzaloğlu**

# Tri-method analysis of contact mechanics in orthotropic-isotropic materials

Received: 27 February 2025 / Accepted: 14 April 2025 / Published online: 9 May 2025
© The Author(s) 2025

**Abstract** This study examines the contact mechanics of a homogeneous orthotropic layer resting on a homogeneous isotropic half-space without being bonded, subjected to loading by a rigid cylindrical punch. The effect of the orthotropic layer's body force has been taken into account in the study. The study is conducted in three phases. In the first phase, the contact problem is analytically tackled using advanced methods such as elasticity theory, integral transform techniques, and Gauss–Chebyshev integration. The second phase utilizes finite element analysis through ANSYS software, accurately modeling the system. In the final phase, an artificial neural network is employed, allowing the system to learn and recognize intricate patterns in the data. The standout feature of this study is its thorough comparison of these three distinct methodologies, offering a comprehensive understanding of the contact mechanics between isotropic and orthotropic materials. The results reveal key insights into contact length, maximum contact stress, critical separation load, and separation distance, all as functions of critical dimensionless parameters. This study is significant in today's advancing field of contact mechanics as it not only explores the combined impact of body forces and the interaction between orthotropic and isotropic materials but also uniquely compares the results using three distinct methods, offering comprehensive insights that address both theoretical and practical challenges.

**Keywords** Contact mechanics · Orthotropic layer · Isotropic half-space · Elasticity theory · Finite element analysis · Artificial neural network

## 1 Introduction

As the name implies, contact mechanics focuses on the stresses and deformations that occur when two solids come into contact. Solids with differing profiles, known as non-conforming, will either make contact at a single point (point contact) or along a line (line contact). Consequently, the contact area between non-conforming solids is relatively small, resulting in stress concentrations near the contact region [1].

The contact region between two solids is influenced by their geometric shapes. In an ideal case, a perfect sphere contacts a flat surface at a single point, while a cylinder establishes contact along a straight line. However, in practical applications, material deformation and inherent geometric imperfections modify this interaction, leading to contact occurring over a finite area rather than a discrete point or line.

E. Öner (✉) · M. G. Oktay
Department of Civil Engineering, Bayburt University, 69000 Bayburt, Turkey
e-mail: eoner@bayburt.edu.tr

E. Uzun Yaylacı
Faculty of Engineering and Architecture, Recep Tayyip Erdogan University, 53100 Rize, Turkey

M. Yaylacı · İrem Mirzaloğlu
Department of Civil Engineering, Recep Tayyip Erdogan University, 53100 Rize, Turkey

Contact mechanics has been a key area of focus in engineering research for more than fifty years. Early work focused primarily on variational inequality formulations, which provided a basic framework for analyzing contact phenomena in a variety of industrial applications. Additionally, early research explored analytical modeling approaches for mechanical systems involving contact, impact and friction, and often used discrete spring-damper models to characterize contact interactions.

In the field of contact mechanics, research is often categorized based on the type of contact, the methods employed, or the material types of the interacting bodies. Studies are typically classified according to the nature of the contact, which includes continuous contact, discontinuous contact, and receding contact problems. Continuous contact involves a constant and uninterrupted interaction between the bodies [2–8], while discontinuous contact is characterized by intermittent or non-continuous interactions [9–12]. Receding contact occurs when the contact area between two solids decreases after a load is applied, resulting in a final contact zone that is smaller than the initial one. This phenomenon typically involves a reduction in the contact region over time or due to specific conditions [13–22].

Additionally, research is classified based on the material types of the contacting bodies. This includes studies on various materials such as isotropic [23–27], transversely isotropic [28–30], orthotropic [31–39], monoclinic [40, 41], and piezoelectric [42–45] materials.

The methods used in contact mechanics studies are also categorized into analytical and numerical approaches. Analytical methods involve deriving exact solutions based on mathematical models and theories, providing precise results for idealized conditions [46–51]. In contrast, numerical methods employ computational techniques to approximate solutions for more complex and realistic scenarios, allowing for the analysis of systems that are difficult to solve analytically [52–62].

In addition to the aforementioned studies, there are several key contributions in the field of contact mechanics that warrant attention. Below, some of the most significant works in this domain are summarized, highlighting their relevance and impact on the development of the field.

The frictional rolling contact between wheels and rails has been addressed in three dimensions using linear elasticity and statics, assuming half-space by Zhao and Li [63]. In multibody dynamics, specifically the evolution of the Hertz contact theory, Machado et al. [64] investigated models of compliant contact forces. A semi-analytical solution is formulated by Zhou and Wei [65] to address the presence of numerous fractures and inhomogeneous inclusions of any shape beneath a half-space surface under contact loading. The planar frictional contact problem of a cylindrical punch over a functionally graded orthotropic medium is studied by Güler et al. [66]. Yaylacı et al. [67] investigated different solution methods for receding contact problems in FG layered mediums. In order to investigate mechanical, thermal, and electrical properties of rough surfaces, Li et al. [68] provide a multi-physics electrical contact model that takes into account the plastic and elastic deformation of asperities. Karabulut et al. [69] developed a frictional moving contact model for an FG orthotropic layer pressed by a rigid cylindrical punch. Öner and Al-Qado [70, 71] have investigated the contact problems of an FG orthotropic layer resting on a rigid foundation for both flat and cylindrical punch cases, considering the scenario in which the external load does not exceed the critical load value. Li et al. [72] investigated the sliding friction contact problems related to the indentation of an elastic half-plane by rigid cylindrical and flat punches within the framework of micropolar theory. Radi et al. [73] investigated the progressive and frictionless contact problem between a rigid circular pin and a circular beam with a uniform cross-section composed of elastic functionally graded material under clearance-fit conditions. Öner and Oktay [74] conducted a semi-analytical analysis of the orthotropic-isotropic contact problem in layered media, taking body forces into account. Zhang et al. [75] analyzed the partial slip contact problem in thermoelectric materials subjected to periodic flat and cylindrical punches.

In this study, we analyze the contact mechanics problem for a system composed of an orthotropic layer and an isotropic half-space using three distinct methods. Our study makes a notable contribution to the field of contact mechanics by addressing a complex problem involving both isotropic and anisotropic materials, analyzed through three distinct methodologies. We employ elasticity theory to provide precise analytical solutions, utilize the Finite Element Method (FEM) via ANSYS software for detailed numerical modeling, and apply Artificial Neural Networks (ANN) for data-driven insights. This multifaceted approach not only enhances the accuracy and depth of the analysis but also explores the impact of body forces within the orthotropic layer, which has been underexplored in existing literature. By integrating these diverse methods, our research offers a comprehensive understanding of the interactions between different material types and the influence of body forces, thereby filling a critical gap in the current knowledge. The novelty of this study lies in its innovative combination of analytical and numerical techniques, which provides new perspectives and practical applications in the realm of contact mechanics.

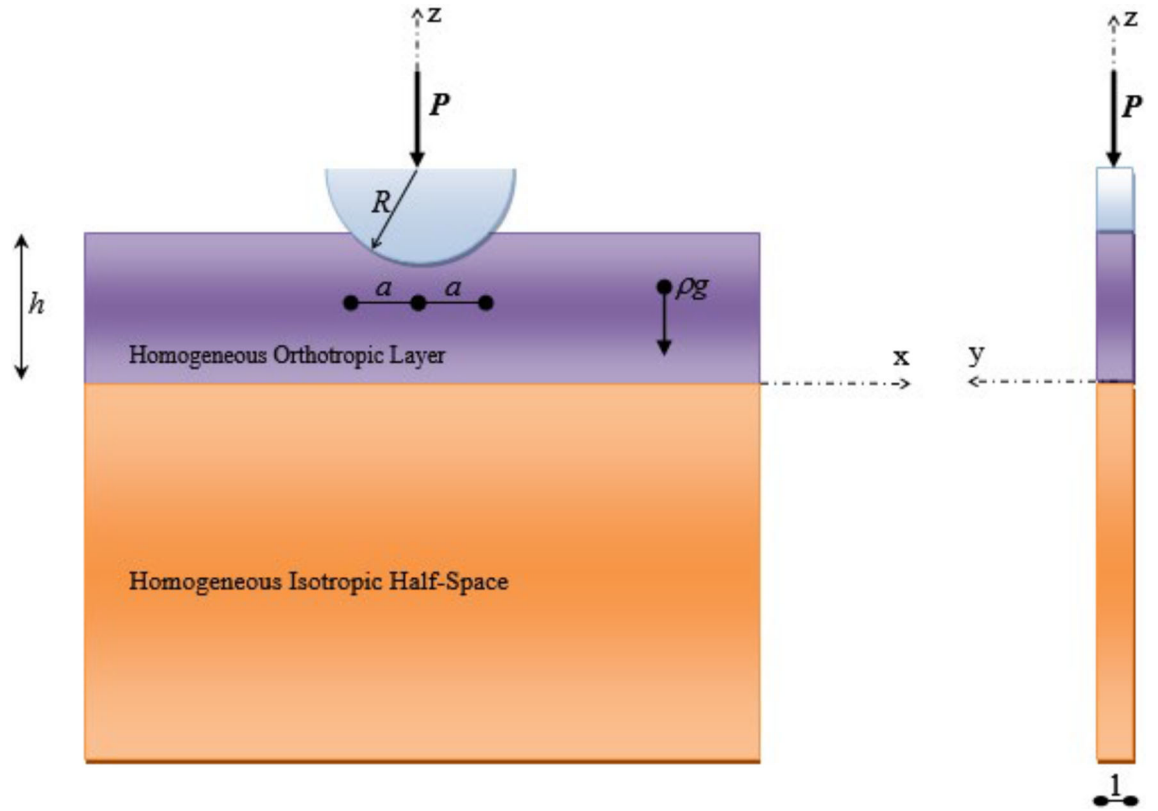


**Fig. 1** Schematic of plane strain continuous contact model with rigid cylindrical punch, orthotropic layer, and isotropic half-space

## 2 Analytical solution of the contact problem

This section details the analytical solution for the contact problem involving a homogeneous orthotropic layer resting on a homogeneous isotropic half-space. The plane strain problem, illustrated schematically in Fig. 1, features a linear elastic, homogeneous orthotropic layer that is not bonded to the underlying homogeneous isotropic half-space and is indented by a rigid cylindrical punch. The punch exerts a normal force $P$ on the orthotropic layer, which has a height $h$. It is assumed that the indentation depth is small enough to induce infinitesimal deformations in the orthotropic layer. As the punch is statically pressed into the layer, points directly beneath the punch move vertically downward, while points away from the punch's axis move radially outward. Additionally, points near the free surface of the orthotropic layer and adjacent to the rigid punch move upward. The semi-contact length, represented as $a$, is illustrated in Fig. 1. The problem solution incorporates vertical body forces acting on the orthotropic layer, and it is assumed that all surfaces are frictionless.

### 2.1 Displacement and stress field analysis in homogeneous orthotropic layer

In the absence of body forces, the equilibrium equations governing plane elastic behavior for a homogeneous orthotropic layer are expressed as follows, where u and w denote the displacement components in the x- and z-directions, respectively:

$$C_{11}\frac{\partial^2 u_{1h}(x,z)}{\partial x^2}+(C_{13}+C_{55})\frac{\partial^2 w_{1h}(x,z)}{\partial x\partial z}+C_{55}\frac{\partial^2 u_{1h}(x,z)}{\partial z^2}=0 \tag{1}$$

$$C_{55}\frac{\partial^2 w_{1h}(x,z)}{\partial x^2}+(C_{13}+C_{55})\frac{\partial^2 u_{1h}(x,z)}{\partial x\partial z}+C_{33}\frac{\partial^2 w_{1h}(x,z)}{\partial z^2}=0 \tag{2}$$

where the subscript 1 for the displacement components $u$ and $w$ represents the homogeneous orthotropic layer, while the subscript $h$ indicates the absence of body forces. $C_{ij}$ are the components of stiffness matrix for orthotropic materials and given in Appendix.

By employing the Fourier sine and cosine transform techniques, the following expressions can be represented as:

$$u_{1h}(x,z) = \frac{2}{\pi}\int_0^\infty \phi_{1h}(\alpha,z)\sin(\alpha x)d\alpha \tag{3}$$

$$w_{1h}(x,z) = \frac{2}{\pi}\int_0^\infty \psi_{1h}(\alpha,z)\cos(\alpha x)d\alpha \tag{4}$$

where the functions $\phi$ and $\psi$ are the inverse transforms of $u$ and $w$, respectively. By differentiating Eqs. (3) and (4) and substituting the results into Eqs. (1) and (2), and then solving the resulting differential equations, the displacement fields for the homogeneous orthotropic layer can be obtained as follows:

$$u_{1h}(x,z) = \frac{2}{\pi}\int_0^\infty \sum_{i=1}^{4} A_i e^{\eta_i \alpha z}\sin(\alpha x)d\alpha \tag{5}$$

$$w_{1h}(x,z) = \frac{2}{\pi}\int_0^\infty \sum_{i=1}^{4} A_i \mho_i e^{\eta_i \alpha z}\cos(\alpha x)d\alpha \tag{6}$$

where the coefficients $A_i$ will be determined based on the boundary conditions of the problem. The expressions $\eta_i$ and $\mho_i$ in (5) and (6) are defined as follows:

$$\eta_i = \mp\frac{\sqrt{\frac{-\Upsilon_2 \pm \sqrt{\Upsilon_2^2 - 4\Upsilon_1\Upsilon_3}}{\Upsilon_3}}}{\sqrt{2}} \tag{7}$$

$$\mho_i = \frac{\eta_i(C_{13}^2 - C_{11}C_{33} + 2C_{13}C_{55} + C_{55}^2 + C_{33}C_{55}\eta_i^2)}{C_{55}(C_{13}+C_{55})}, \qquad (i = 1,...,4) \tag{8}$$

where

$$\Upsilon_1 = C_{11}C_{55} \tag{9}$$

$$\Upsilon_2 = 2C_{13}C_{55} + C_{13}^2 - C_{11}C_{33} \tag{10}$$

$$\Upsilon_3 = C_{33}C_{55} \tag{11}$$

By applying Hook's law alongside Eqs. (5) and (6), the stress fields for the orthotropic layer are derived as follows:

$$\sigma_{1zh}(x,z) = \frac{2}{\pi}\int_0^\infty \alpha \sum_{i=1}^{4} A_i(C_{13} + C_{33}\mho_i\eta_i)e^{\eta_i\alpha z}\cos(\alpha x)d\alpha \tag{12}$$

$$\tau_{1xzh}(x,z) = \frac{2}{\pi}\int_0^\infty \alpha \sum_{i=1}^{4} A_i C_{55}(\eta_i - \mho_i)e^{\eta_i\alpha z}\sin(\alpha x)d\alpha \tag{13}$$

For a homogeneous orthotropic layer, when the body forces are set to $F_x = 0$ and $F_z = \rho g$, the equilibrium equations can be expressed as follows:

$$C_{11}\frac{\partial^2 u_{1p}}{\partial x^2} + C_{55}\frac{\partial^2 u_{1p}}{\partial z^2} + (C_{13}+C_{55})\frac{\partial^2 w_{1p}}{\partial x \partial z} = 0 \tag{14}$$

$$C_{55}\frac{\partial^2 w_{1p}}{\partial x^2} + C_{33}\frac{\partial^2 w_{1p}}{\partial z^2} + (C_{13}+C_{55})\frac{\partial^2 u_{1p}}{\partial x \partial z} = \rho g \tag{15}$$

where $\rho$ represents the density of the orthotropic layer, $g$ denotes the gravitational acceleration, and the subscript $p$ in the displacement components indicates the scenario where body forces are present.

To determine the specific solution for the displacement and stress fields in the orthotropic layer subjected solely to vertical body forces, the following approach is used: The specific solution for the orthotropic layer, characterized by a unit weight $\rho g$, height $h$, and resting on either a rigid or elastic flat surface, is obtained by assuming the displacements $u_{1p} = u_{1p}(x)$ and $w_{1p} = w_{1p}(z)$ [76]. Based on these assumptions, the equilibrium equations can be written as follows:

$$C_{11}\frac{\partial^2 u_{1p}(x)}{\partial x^2} = 0 \tag{16}$$

$$C_{33}\frac{\partial^2 w_{1p}(z)}{\partial z^2} = \rho g \tag{17}$$

For the orthotropic layer under the influence of vertical body forces alone, the displacement fields are derived by solving Eqs. (16) and (17), while Hooke's law is used to compute the corresponding stress fields. To determine the integral constants that arise from these displacement and stress fields, the following boundary conditions are utilized:

$$u_{1p}(0) = 0 \tag{18}$$

$$w_{1p}(0) = 0 \tag{19}$$

$$\sigma_{1zp}(z) = -\rho g(h - z) \tag{20}$$

$$\int_0^h \sigma_{1xp} dz = 0 \tag{21}$$

Given the preceding information, the displacement and stress fields of the orthotropic layer, when subjected exclusively to body forces, are:

$$w_{1p}(z) = \frac{\rho g}{2C_{33}}\frac{gh\rho(-C_{13}^2 + 2C_{11}C_{33})}{2C_{33}(-C_{13}^2 + C_{11}C_{33})}z^2 \tag{22}$$

$$\sigma_{1zp}(z) = -\frac{gh\rho C_{13}^2}{2(C_{13}^2 - C_{11}C_{33})} - \frac{gh\rho(-C_{13}^2 + 2C_{11}C_{33})}{2(-C_{13}^2 + C_{11}C_{33})} + \rho g z \tag{23}$$

$$\tau_{1xzp} = 0 \tag{24}$$

Consequently, the displacement and stress fields for the orthotropic layer are determined by combining the specific solution with the homogeneous solution. This approach leads to the following expressions:

$$w_1(x, z) = w_{1h}(x, z) + w_{1p}(z) \tag{25}$$

$$\sigma_{1z}(x, z) = \sigma_{1zh}(x, z) + \sigma_{1zp}(z) \tag{26}$$

$$\tau_{1xz}(x, z) = \tau_{1xzh}(x, z) + \tau_{1xzp} \tag{27}$$

## 2.2 Displacement and stress field analysis in homogeneous isotropic half-space

The equilibrium equations for the isotropic half-space, in the absence of body forces, are as follows:

$$(\lambda_2 + \mu_2)\frac{\partial}{\partial x}\left(\frac{\partial u_2(x, z)}{\partial x} + \frac{\partial w_2(x, z)}{\partial z}\right) + \mu_2\left(\frac{\partial^2 u_2(x, z)}{\partial x^2} + \frac{\partial^2 u_2(x, z)}{\partial z^2}\right) = 0 \tag{28}$$

$$(\lambda_2 + \mu_2)\frac{\partial}{\partial z}\left(\frac{\partial u_2(x, z)}{\partial x} + \frac{\partial w_2(x, z)}{\partial z}\right) + \mu_2\left(\frac{\partial^2 w_2(x, z)}{\partial x^2} + \frac{\partial^2 w_2(x, z)}{\partial z^2}\right) = 0 \tag{29}$$

where the Lamé constants are represented by $\lambda_2$ and $\mu_2$. In Eqs. (28) and (29), the isotropic half-space is indicated by the subscript "2". The displacement fields of the isotropic half-space can be obtained by following

the procedures detailed in the previous section, which include using Fourier sine and cosine integral transforms for the displacement fields and executing the corresponding intermediate calculations.

$$u_2(x,z) = \frac{2}{\pi}\int_0^\infty \left[(B_1 + B_2 z)e^{\alpha z}\right]\sin(\alpha x)d\alpha \tag{30}$$

$$w_2(x,z) = \frac{2}{\pi}\int_0^\infty \left[\left[-B_1 + \left(\frac{\kappa_2}{\alpha} - z\right)B_2\right]e^{\alpha z}\right]\cos(\alpha x)d\alpha \tag{31}$$

In Eq. (31), the Kolosov's constant for the isotropic half-space is represented by $\kappa_2$, where $\kappa_2$ = 3-4$\upsilon_2$ under plane strain condition. $\upsilon_2$ is the Poisson's ratio of the isotropic half-space. With this definition and using Hooke's Law, the stress fields for the isotropic half-space can be formulated as:

$$\frac{1}{2\mu_2}\sigma_{2z}(x,z) = \frac{2}{\pi}\int_0^\infty \left[-\alpha(B_1 + B_2 z) + \left(\frac{1+\kappa_2}{2}\right)B_2\right]e^{\alpha z}\cos(\alpha x)d\alpha \tag{32}$$

$$\frac{1}{2\mu_2}\tau_{2xz}(x,z) = \frac{2}{\pi}\int_0^\infty \left[\alpha(B_1 + B_2 z) + \left(\frac{1-\kappa_2}{2}\right)B_2\right]e^{\alpha z}\sin(\alpha x)d\alpha \tag{33}$$

When determining the stress and displacement fields for homogeneous half-space, it was considered that, according to the axis configuration in Fig. 1, the stresses and displacements can only be zero as z → -∞ if the coefficients of $e^{-\alpha z}$ are zero. The coefficients $B_1$ and $B_2$ appearing in Eqs. (30), (31), (32) and (33) will be determined based on the boundary conditions of the problem.

### 2.3 Boundary conditions and solution of integral equation

The boundary conditions relevant to the contact problem described earlier are as follows:

$$\tau_{1xz}(x,h) = 0 \qquad (0 \le x < \infty) \tag{34}$$

$$\sigma_{1z}(x,h) = \left\{\begin{array}{lll} -p(x) & ; & (0 \le x < a) \\ 0 & ; & (a \le x < \infty)\end{array}\right\} \tag{35}$$

$$\tau_{1xz}(x,0) = 0 \qquad (0 \le x < \infty) \tag{36}$$

$$\tau_{2xz}(x,0) = 0 \qquad (0 \le x < \infty) \tag{37}$$

$$\sigma_{1z}(x,0) = \sigma_{2z}(x,0) \qquad (0 \le x < \infty) \tag{38}$$

$$\frac{\partial}{\partial x}[w_1(x,0) - w_2(x,0)] = 0 \qquad (0 \le x < \infty) \tag{39}$$

In Eq. (35), *p(x)* denotes the contact stress within the region $(-a, +a)$, where the orthotropic layer interacts with the rigid cylindrical punch. The six unknown functions $A_i$ (i = 1,…4) and $B_j$ (j = 1,2) can be determined using the six equations derived from the boundary conditions in Eqs. (34), (35), (36), (37), (38), and (39). By substituting the expressions for the transformed displacements and stresses and converting them into Fourier space, we obtain

$$A_i = \frac{1}{E_x}\int_0^a p(t)\mathrm{Cos}(\alpha t)A_i^K dt, \qquad (i = 1,...,4) \tag{40}$$

$$B_j = \frac{1}{E_x}\int_0^a p(t)\mathrm{Cos}(\alpha t)B_j^K dt, \qquad (j = 1,2) \tag{41}$$

Due to the extensive length of the mathematical expressions for the coefficients $A_i^K$ and $B_j^K$, they will not be included in the manuscript. It is important to highlight that the stationary contact stress *p(x)* remains unknown in the solutions presented above. As demonstrated below, it must be determined by applying the displacement continuity condition along the stationary contact interface.

$$\frac{\partial}{\partial x} w_1(x,h) = \frac{x}{R} \tag{42}$$

where $R$ is the radius of the rigid cylindrical punch. Substituting $A_i$ into condition (42) results in the following singular integral equation.

$$\frac{1}{\pi} \int_{-a}^{a} \left[ \frac{1}{t-x} + \Gamma(x,t) \right] p(t)dt = \frac{E_x}{\Lambda} \frac{x}{R} \tag{43}$$

where $\Gamma(x,\ t)$ denotes the kernel of the singular integral equation, and $\Lambda$ represents the singular term, with both details given in the Appendix.

Moreover, the equilibrium condition requires that the stress resultant transmitted through the contact interface must be equal to the indentation force.

$$\int_{-a}^{a} \sigma_{1z}(x,h)dx = \int_{-a}^{a} p(t)dt = P \tag{44}$$

The continuous contact condition is valid only when the external load remains within the range from zero to the critical load ($P_{cr}$), which is yet to be determined. In order to determine both the critical separation load and the critical separation distance, it is necessary to evaluate the contact stresses between the orthotropic layer and the isotropic half-space, ensuring that the contact stress becomes zero at the point of separation. By substituting the coefficients $A_i$ (i = 1,…,4) into Eq. (26), the contact stress at the interface can be accurately computed as follows:

$$\sigma_{1z}(x,0) = \frac{1}{\pi} \int_{-a}^{a} \zeta(x,t)p(t)dt - \rho g h = 0 \tag{45}$$

where $\zeta(x,\ t)$ is the kernels of the $\sigma_{1z}(x,\ 0)$ and given in Appendix.

Analytical solution for the singular integral Eq. (43) is not available, necessitating the development of a numerical scheme. To move forward, we introduce the following dimensionless parameters and functions:

$$x = ar, \tag{46}$$

$$t = as, \tag{47}$$

$$\mathrm{Z}(s) = \frac{p(as)}{E_x} \tag{48}$$

Through the application of the normalizations in (46), (47) and (48), the integral Eq. (43), the equilibrium condition (44), and the contact stress across the interface (45) can be formulated as follows:

$$\frac{1}{\pi} \int_{-1}^{1} \left[ \frac{1}{s-r} + \frac{a}{h}\Gamma(r,s) \right] \mathrm{Z}(s)ds = \frac{1}{\Lambda} \frac{a/h}{R/h} r \tag{49}$$

$$\frac{a}{h} \int_{-1}^{1} \mathrm{Z}(s)ds = \frac{P}{E_x h} \tag{50}$$

$$\frac{\sigma_{1z}(x,0)}{E_x} = \frac{1}{\pi} \frac{a}{h} \int_{-1}^{1} \zeta(x,as)\mathrm{Z}(s)ds - \frac{\rho g h}{E_x} = 0 \tag{51}$$

According to Erdoğan and Gupta [77], the index of the integral Eq. (49) is − 1, owing to the fact that the contact stresses become zero at the boundary of the contact region. The solution for the integral Eq. (49) can be formulated as:

$$Z(s) = \Xi(s)/(1-s^2)^{-1/2} \tag{52}$$

The Gauss–Chebyshev integration formula is applied to convert Eqs. (49), (50) and (51) into the subsequent system of algebraic equations.

$$\sum_{k=1}^{N} W_k \left[ \frac{1}{s_k - r_i} + \frac{a}{h}\Gamma(r_i, s_k) \right] \Xi(s_k) = \frac{1}{\Lambda}\frac{a/h}{R/h} r_i, \qquad (i = 1, ..., N+1) \tag{53}$$

$$\frac{a}{h}\sum_{k=1}^{N} W_k \, \Xi(s_k) = \frac{1}{\pi}\frac{P}{E_x h} \tag{54}$$

$$\frac{\sigma_{1z}(x,0)}{E_x} = \frac{a}{h}\sum_{k=1}^{N} W_k \zeta(r_i, s_k)\Xi(s_k) - \frac{\rho g h}{E_x} = 0 \tag{55}$$

where

$$W_k = \frac{1-s_k^2}{N+1}, \tag{56}$$

$$r_i = \mathrm{Cos}\left(\frac{2i-1}{N+1}\frac{\pi}{2}\right), \tag{57}$$

$$s_k = \mathrm{Cos}\left(\frac{k\pi}{N+1}\right). \tag{58}$$

Due to the symmetry of the contact between the rigid punch and the orthotropic layer, the (N/2 + 1)$^{th}$ equation in (53) is automatically fulfilled. Consequently, for a total of N + 2 unknowns—N contact stress values, *a/h* (the normalized contact length), and *P/(E$_x$h)* (load factor)—a corresponding system of N + 2 equations is obtained: N equations, the equilibrium condition (54), and Eq. (55). These unknowns will be determined iteratively. Furthermore, the solution must ensure that the contact stress between the layers remains compressive, as specified in the following condition.

$$Max\left[\frac{\sigma_{1z}(x,0)}{E_x}\right] \le 0 \tag{59}$$

To begin iterative process, initial estimates for *a/h* and *P/(E$_x$h)* are made, after which the system of equations from (53) is solved to compute $\Xi(s_k)$. Subsequently, the conditions in (54), (55) and (59) are verified. The iterative process is repeated until the required accuracy for these conditions is reached. The value of *P/(E$_x$h)* that satisfies condition (55) defines the critical separation load $P_{cr}/(E_x h) = \lambda_{cr}$, while the corresponding *x/h* denotes the critical separation distance ($x_{cr}/h$). A precision of $10^{-6}$ is chosen for this analysis, and the iteration process is carried out using the Newton–Raphson method to ensure convergence.

## 3 Finite element analysis of the problem

The finite element method (FEM), renowned for its extensive application across various scientific and engineering disciplines, is particularly effective in addressing contact problems. FEM is especially adept at analyzing the interactions between materials, even in complex geometries. Advances in technology have led to the development of sophisticated software tools that enable detailed specification of material properties and the design of mesh models with diverse element configurations. These advancements have enhanced the precision of FEM analyses, resulting in highly realistic outcomes and extensive research on contact phenomena. Analytical solutions and finite element method (FEM) based solutions have been concurrently investigated and compared. This comparative approach is frequently observed in the literature, as it aims to achieve a more accurate and realistic numerical analysis method [78–80].

In this section of the study, a finite element method (FEM) solution was developed using ANSYS software [81]. The analysis involves an orthotropic layer, an isotropic half-space and a cylindrical punch. The geometric

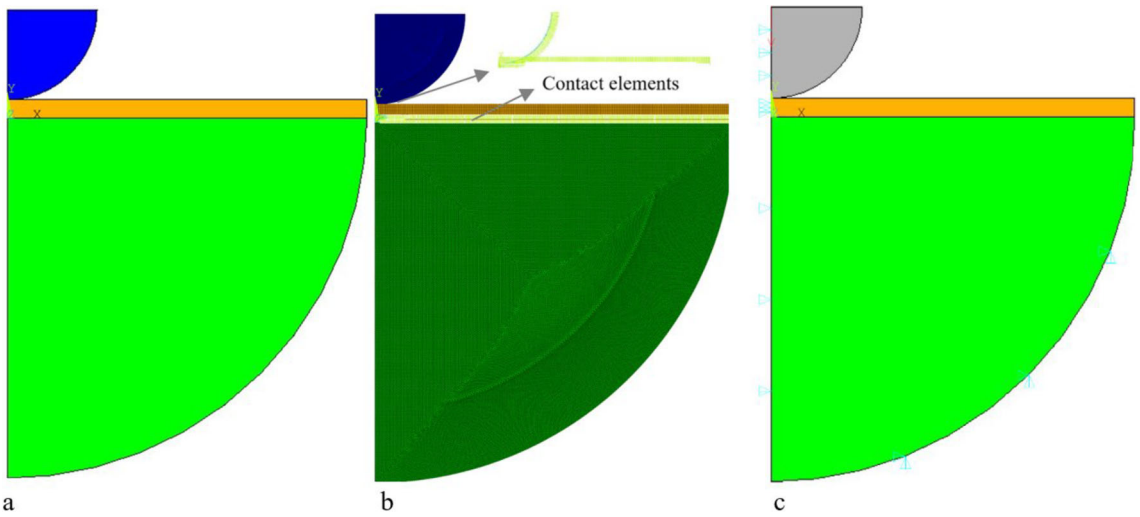


**Fig. 2** Finite element model overview, **a** geometric configuration, **b** mesh design, **c** loads, and boundary conditions

**Table 1** Test parameters

| R/h | | $\frac{P/h}{E_x}$ | | $E_2/E_x$ | | Material type |
|---|---|---|---|---|---|---|
| 10 | 125 | 0.00005 | 0.0075 | 0.05 | 3 | B/Al |
| 20 | 150 | 0.001 | 0.0085 | 0.1 | 4 | Gr/Al |
| 50 | 200 | 0.0025 | 0.01 | 0.5 | 10 | Gl/Ep |
| 80 | 300 | 0.005 | 0.0125 | 1 | $\infty$ | Gr/Ep-T |
| 100 | | | | 2 | | Gr/Ep-P |

properties of the contact problem were initially defined as depicted in Fig. 2a. The modeling was carried out in two dimensions, focusing on the orthotropic layer, where L = 50 m denotes the length in the x-direction and h = 1 m denotes the height in the z-direction. Due to the symmetry of the problem geometry and applied loadings, modeling only half of the system was deemed sufficient.

In the second phase, the mesh structure for the geometric model was established. The accuracy of finite element method (FEM) simulations heavily relies on the alignment of the mesh elements with the geometric model and the total number of elements utilized. To ensure realistic modeling, the mesh was generated with 88,751 elements and 168,727 nodes, based on empirical testing. The PLANE183 element, which offers two degrees of freedom and is well-suited for complex and irregular mesh configurations, was selected for structural analysis. In the contact region, a total of 700 CONTA172 and TARGE169 elements, known for their compatibility, were defined. The mesh structure for the contact problem is illustrated in Fig. 2b. Loading was done from the top point of the punch. As for the boundary conditions, the symmetrical boundary condition in the z-axis and half-space was fixed on all axes from the bottom surface (Fig. 2c). The analysis was completed by applying the specified material properties, loads, and boundary conditions. The resulting deformation and contact stress are depicted in Fig. 3.

## 4 Investigation of the problem using artificial neural networks (ANNs)

Artificial neural networks (ANNs) which are capable of learning, recognizing, and predicting are employed to address nonlinear relationships between data. ANNs can be trained through two primary methods: supervised and unsupervised learning. In this study, a supervised learning approach, specifically the multilayer perceptron, was utilized. The network was designed using the BFGS (Broyden–Fletcher–Goldfarb–Shanno) algorithm to forecast the contact length, maximum contact stress, critical separation load, and critical separation distance. The training dataset was generated by theoretically solving various combinations of the data presented in Table 1. Network models were developed employing four different processing patterns. These input variables are,

*R/h:* punch radius.

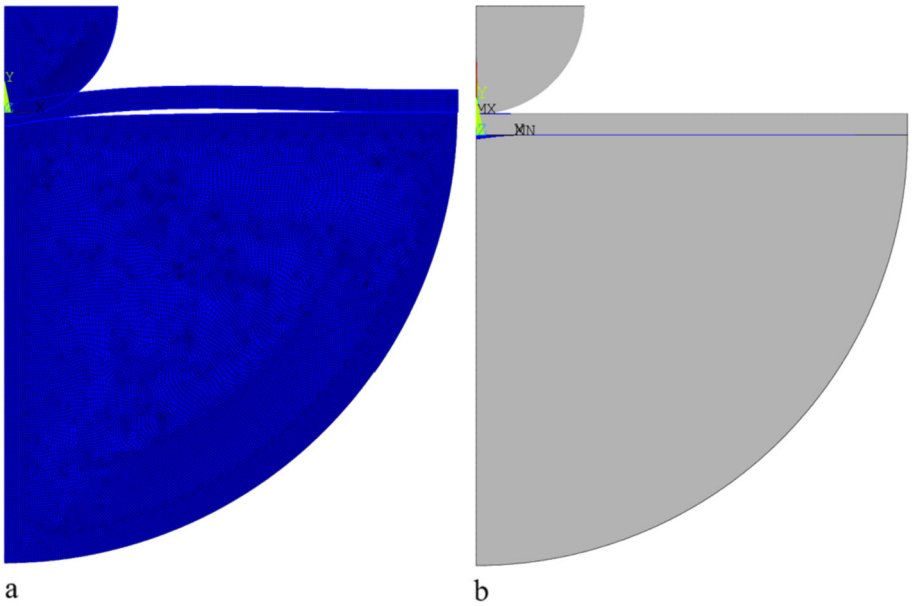


**Fig. 3** Post-analysis images, **a** deformation shape, **b** contact stress

$\frac{P/h}{E_x}$: applied load.
*Material type*
$E_2/E_x$: dimensionless elastic modulus of isotropic half-space.
The output layer of the network consists of four process patterns. These output variables are,
*a/h:* contact length.
$max[p(x)/E_x]$: maximum contact stress.
$\lambda_{cr}$: critical separation load.
$x_{cr}/h$: critical separation distance.

In this study, Statistica software 12 (StatSoft Inc., OK, USA) was utilized for data processing and the design of artificial neural networks (ANNs). The input data were randomly partitioned into three subsets by the software: 70% for training, 15% for testing, and 15% for validation. The configuration of the hidden layers and the number of neurons were determined through iterative trial and error, while weight values were initially assigned randomly within the range of 0.0001 to 0.001. The performance of two error functions—sum of squares and entropy—was compared to evaluate their suitability for the system. Subsequently, various network activation functions, including Identity, logistic sigmoid, hyperbolic tangent, exponential, softmax, and Gaussian were employed to facilitate signal transmission between layers. A total of 7200 networks were trained and retrained. Additionally, the program code was rewritten in C + + to compute the contact length, maximum contact stress, critical separation load, and critical separation distance.

## 5 Results and discussion

In this paper, the contact mechanics problem between a homogeneous orthotropic layer and a homogeneous isotropic half-space is analyzed using three different approaches: analytically based on elasticity theory, numerically via the finite element method (FEM), and through an artificial neural network (ANN) model. The analyses yielded normalized results for contact length, maximum contact stress, critical separation load, and critical separation distance. The findings demonstrated that the ANN and FEM methods provided highly accurate results for the specified parameters. The elastic properties of the orthotropic materials used in this study are based on the work of Binienda and Pindera [82]. Their research provides a comprehensive framework for the material properties employed in this analysis.

This study explores the potential of neural network analysis in predicting key parameters of contact mechanics, including contact length, maximum contact stress, critical separation load, and critical separation distance. The artificial neural network (ANN) model, utilizing a sum-of-squares (SOS) error term, yielded superior

**Table 2** Key features of ANNs for output element recognition

| Network | MLP | Error in learning (%) | Error in testing (%) | Error in validation (%) | Learning algorithm | Error function | Activation function inhidden layer | Activation function in output layer |
|---|---|---|---|---|---|---|---|---|
| N1 | 4-11-4 | 1.13 | 0.4 | 0 | BFGS 133 | SOS | Tanh | Exponential |
| N2 | 4-11-4 | 1.56 | 0 | 0.1 | BFGS 236 | SOS | Tanh | Identity |
| N3 | 4-11-4 | 4.33 | 1.91 | 4.1 | BFGS 456 | SOS | Tanh | Identity |
| N4 | 4-11-4 | 0 | 0 | 0 | BFGS 404 | SOS | Tanh | Identity |

*BFGS* Broyden fletcher goldfarb shanno algorithm, *SOS* sum of square, *Tanh* hyperbolic tangent function

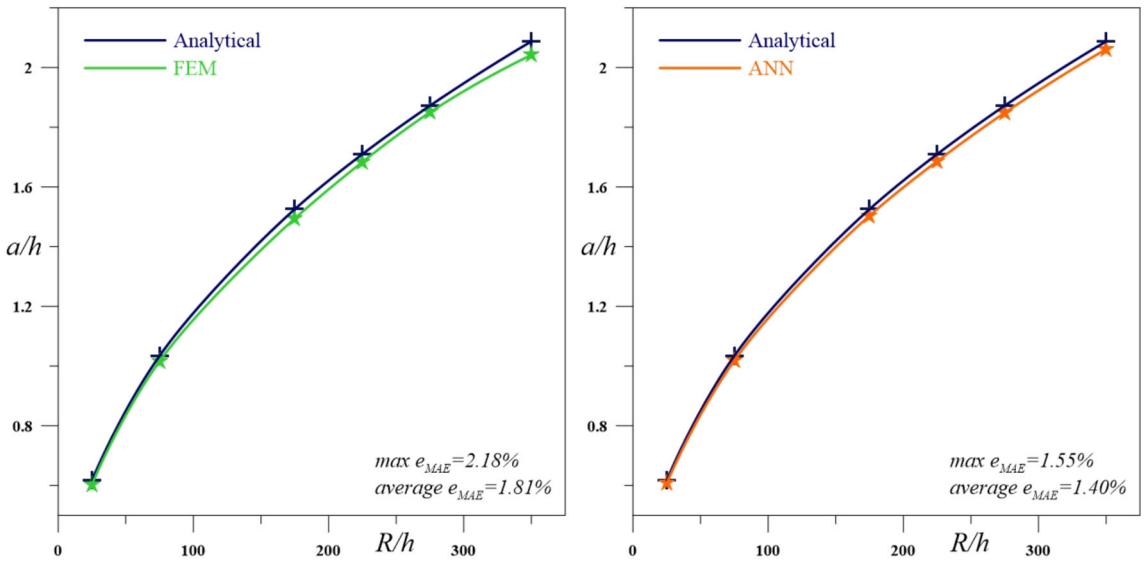


**Fig. 4** Variation of contact length with changing punch radius [(P/h)/$E_x$ = 0.001, $\kappa_2 = 2$, $\mu_2 = 10$, Gr/Ep(P75/934)]

performance. The optimal network architecture comprised 11 units per hidden layer, with a hyperbolic tangent (Tanh) activation function. The performance of the best networks is summarized in Table 2. The results indicate that the developed ANN model effectively and efficiently estimates contact stresses and lengths, demonstrating a high level of accuracy and reliability in predicting these critical parameters.

The agreement between the numerical and analytical results was assessed using the mean absolute error ($e_{MAE}$). The $e_{MAE}$ serves as a suitable metric for evaluating the performance of both FEM and ANN results and is defined by the following equation.

$$e_{MAE}(\%) = \left| \frac{R_{A_i} - R_{FEM_i} \text{ or } R_{ANN_i}}{R_{A_i}} \right| \times 100 \qquad (i = 1, 2, 3, ..., n) \tag{60}$$

where $R_{A_i}$ represents the analytical results, while $R_{FEM_i}$ and $R_{ANN_i}$ correspond to the numerical results for normalized contact length, contact stress, critical separation load, and critical separation distance. The variable $n$ denotes the total number of results.

Figures 4, 5, 6, 7, 8, 9, 10, 11, 12, 13, 14, 15, 16, 17 and 18 present the dimensionless results obtained from the parametric analysis of the contact mechanics problem between a homogeneous orthotropic layer, indented by a rigid cylindrical punch, and a homogeneous isotropic half-space. In these figures, the results derived from the analytical method are compared with those obtained from numerical approaches, including FEM and ANN, providing a comprehensive evaluation of the methodologies.

Figure 4 illustrates the effect of punch radius on the contact length at the interface between the punch and the orthotropic layer. The figure shows that an increase in punch radius leads to a proportional increase in contact length, resulting in a broader contact area between the two media. This behavior is consistent with the expected physical phenomena. A comparison between the analytical solution and the numerical methods (FEM and ANN) reveals maximum relative errors (max $e_{MAE}$) for contact length 2.18% and 1.55%, respectively.

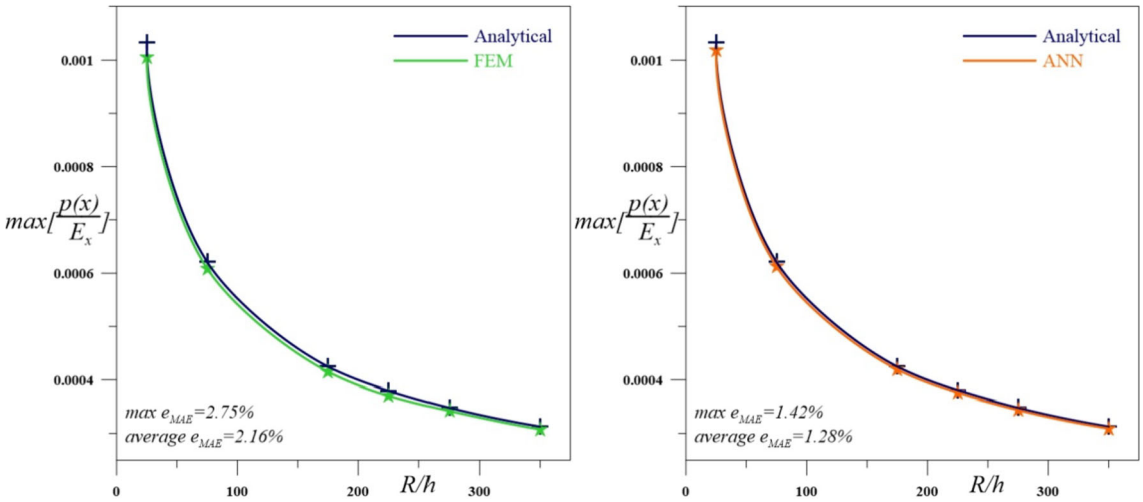


**Fig. 5** Variation of maximum contact stress with changing punch radius [(P/h)/$E_x$ = 0.001, $\kappa_2 = 2$, $\mu_2 = 10$, Gr/Ep(P75/934)]

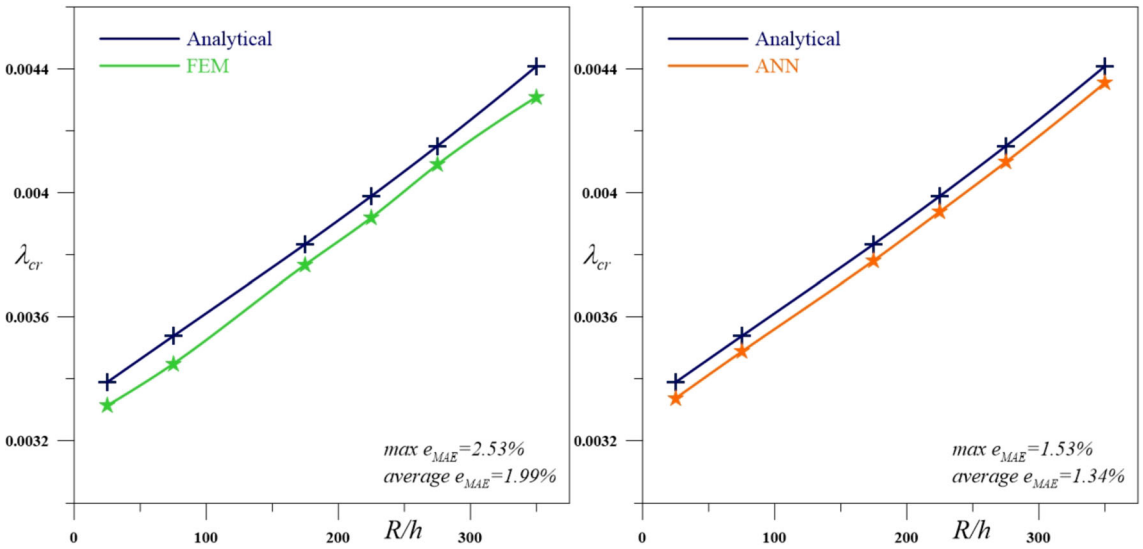


**Fig. 6** Effect of punch radius on critical separation load [(P/h)/$E_x$ = 0.001, $\kappa_2 = 2$, $\mu_2 = 10$, Gr/Ep(P75/934)]

The average relative error for FEM is calculated as 1.81%, while for ANN it is 1.40%, indicating a high level of accuracy in both numerical approaches.

Figure 5 demonstrates the influence of punch radius on the maximum contact stress at the interface between the punch and the orthotropic layer. As the figure shows, an increase in punch radius distributes the load over a larger area, leading to a reduction in maximum contact stress. This outcome aligns with the expected physical behavior of stress distribution. When comparing the analytical method with the numerical approaches (FEM and ANN), the maximum relative errors and average relative errors for maximum contact stress are computed as $e_{MAE(FEM)} = 2.75\%$, $e_{MAE(ANN)} = 1.42\%$ and $e_{MAE(FEM)} = 2.16\%$,$e_{MAE(ANN)} = 1.28\%$, respectively.

Figure 6 depicts the effect of punch radius on the critical separation load which initiates the first separation between the orthotropic layer and the isotropic half-space. The figure shows that as the punch radius increases, the critical load required for separation also increases. In other words, a larger punch radius requires a higher load to initiate separation. A comparison of the analytical method with the numerical approaches (FEM and ANN) reveals maximum relative errors $e_{MAE(FEM)} = 2.53\%$,$e_{MAE(ANN)} = 1.53\%$, while the average relative errors are $e_{MAE(FEM)} = 1.99\%$,$e_{MAE(ANN)} = 1.34\%$, demonstrating good consistency between the methods.

Figure 7 examines the effect of punch radius on the distance of critical separation between the orthotropic layer and the isotropic half-space. The figure indicates that an increase in punch radius results in the initial

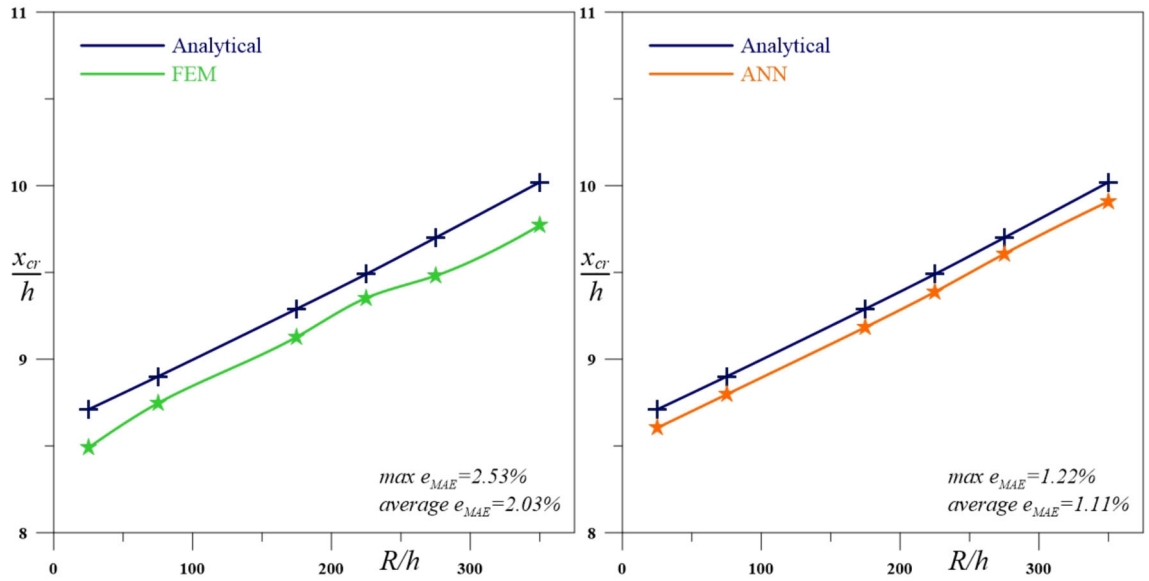


**Fig. 7** Effect of punch radius on critical separation distance [(P/h)/$E_x$ = 0.001, $\kappa_2 = 2$, $\mu_2 = 10$, Gr/Ep(P75/934)]

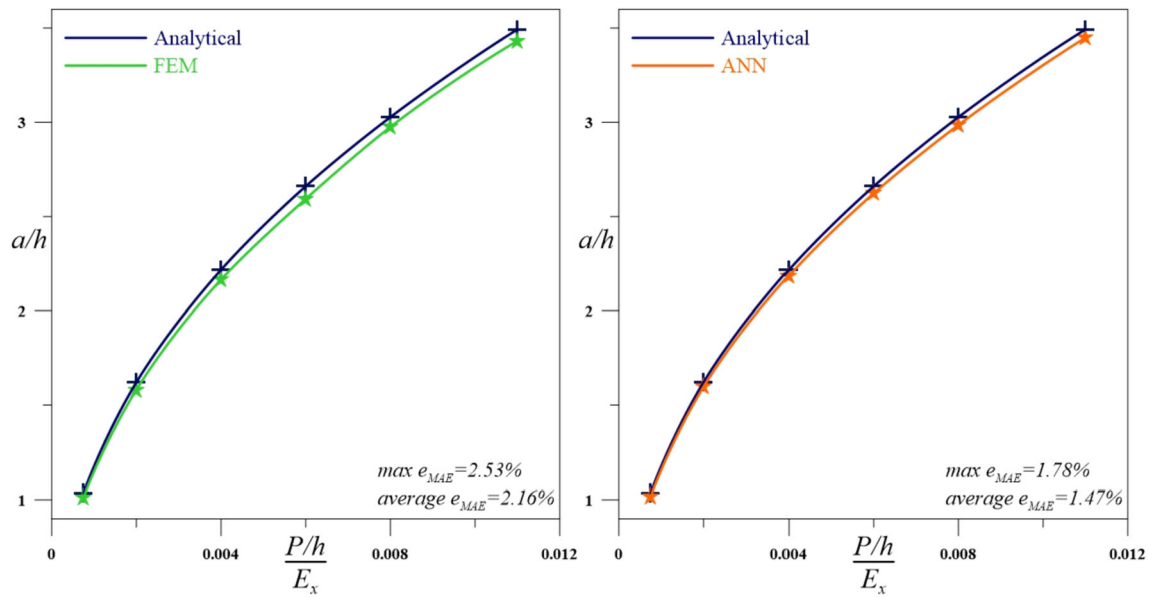


**Fig. 8** Variation of contact length depending on the applied load [R/h = 100, $\kappa_2 = 2$, $\mu_2 = 10$, Gr/Ep(P75/934)]

separation point moving farther from the axis of symmetry. A comparison between the analytical method and numerical approaches (FEM and ANN) shows that the maximum relative errors are $e_{MAE(FEM)} = 2.53\%$ and $e_{MAE(ANN)} = 1.22\%$, while the average relative errors are $e_{MAE(FEM)} = 2.03\%$ and $e_{MAE(ANN)} = 1.11\%$. These results highlight the accuracy and consistency of the analytical and numerical methods in predicting the distance of critical separation.

Figure 8 illustrates how the contact length at the interface between the punch and the orthotropic layer is affected by the applied load. As the applied load increases, the punch penetrates further into the orthotropic layer, resulting in a corresponding increase in contact length. Comparing the analytical method with numerical approaches (FEM and ANN), the maximum relative errors in contact length are found to be $e_{MAE(FEM)} = 2.53\%$ and $e_{MAE(ANN)} = 1.78\%$, while the average relative errors are $e_{MAE(FEM)} = 2.16\%$ and $e_{MAE(ANN)} = 1.47\%$, respectively.

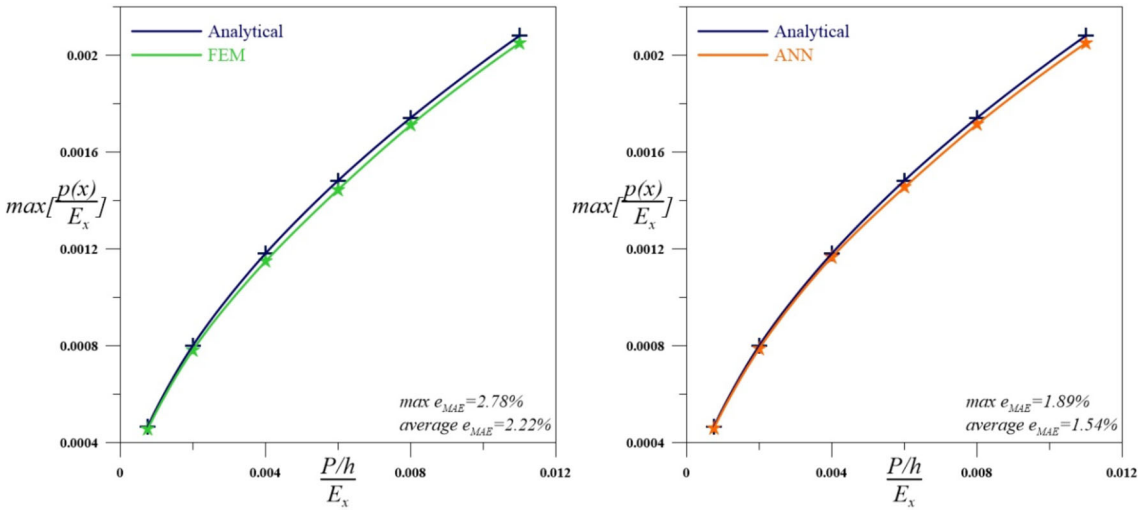


**Fig. 9** Variation of maximum contact stress depending on the applied load [R/h = 100, $\kappa_2 = 2$, $\mu_2 = 10$, Gr/Ep(P75/934)]

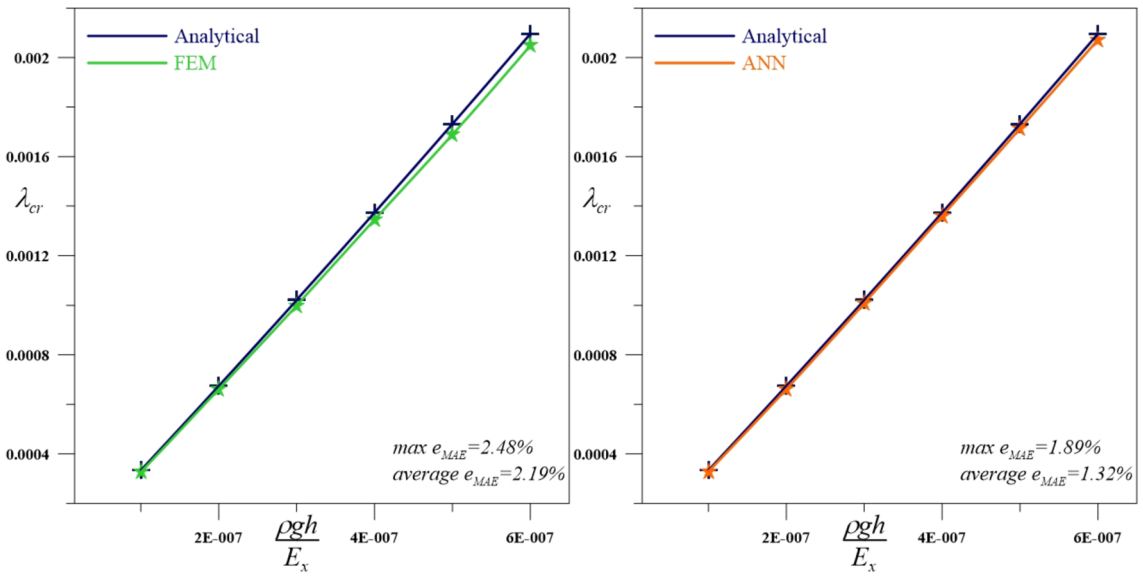


**Fig. 10** Impact of orthotropic layer's body force on critical separation load [R/h = 100, $\kappa_2 = 2$, $\mu_2 = 10$, Gr/Ep(P75/934)]

Figure 9 shows how the applied load influences the maximum stress at the contact interface between the punch and the orthotropic layer. As depicted, an increase in the applied load results in a corresponding rise in maximum contact stress. Comparing the analytical method with numerical approaches (FEM and ANN), the maximum relative errors in maximum contact stress are $e_{MAE(FEM)} = 2.78\%$ and $e_{MAE(ANN)} = 1.89\%$, while the average relative errors are $e_{MAE(FEM)} = 2.22\%$ and $e_{MAE(ANN)} = 1.54\%$.

In Fig. 10, the variation of the critical separation load which causes the initial separation between the orthotropic layer and the isotropic half-space is examined in relation to the body force of the orthotropic layer. The figure shows that an increase in the body force of the orthotropic layer, which corresponds to the layer becoming heavier, leads to an increase in the critical load required to achieve the initial separation. In other words, a greater load is needed to separate a heavier layer from the isotropic half-space. Comparing the analytical method with the numerical approaches (FEM and ANN), the maximum relative errors for critical separation load are $e_{MAE(FEM)} = 2.48\%$ and $e_{MAE(ANN)} = 1.89\%$, while the average relative errors are $e_{MAE(FEM)} = 2.19\%$ and $e_{MAE(ANN)} = 1.32\%$.

Figure 11 illustrates the influence of the different orthotropic materials on the contact length at the interface between the punch and the orthotropic layer. A key consideration when assessing the impact of material

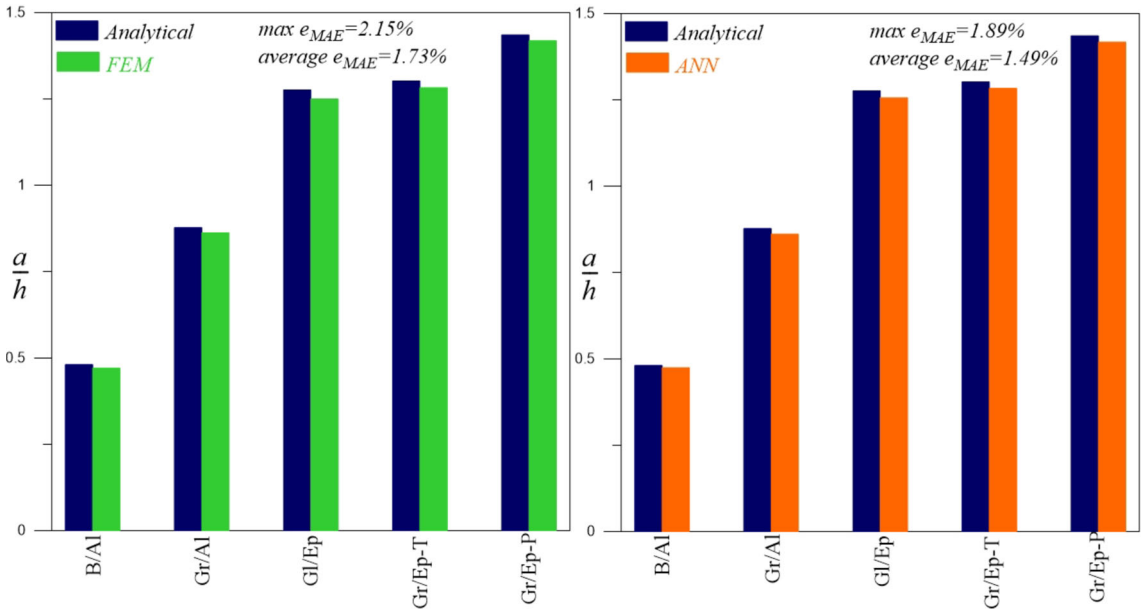


**Fig. 11** Variation of contact length depending on the use of different orthotropic materials ($E_2/E_x = 1, \kappa_2 = 2, E_x = 42.7$, $(P/h)/E_x = 0.003$, $R/h = 80$)

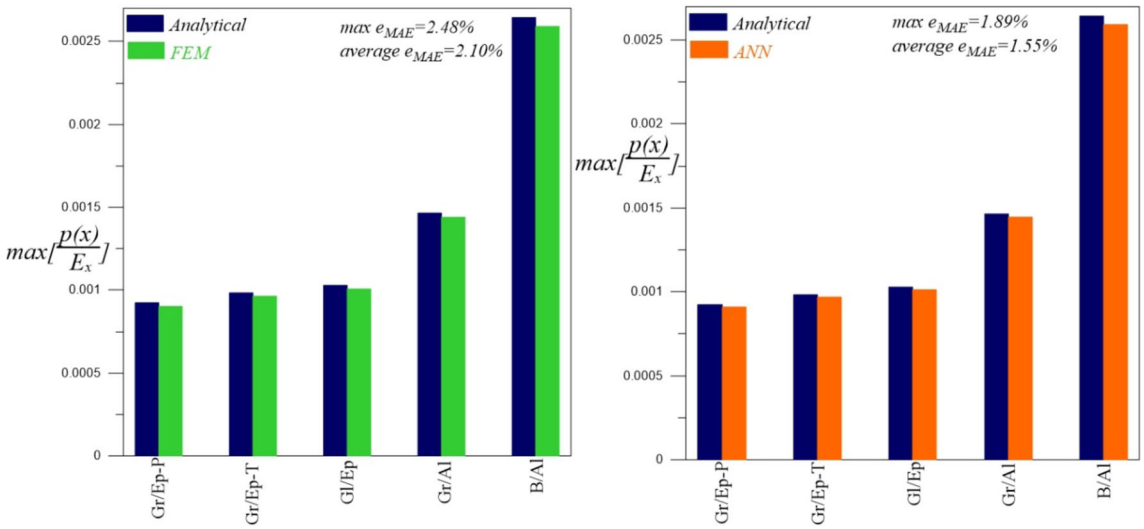


**Fig. 12** Variation of maximum contact stress depending on the use of different orthotropic materials ($E_2/E_x = 1, \kappa_2 = 2, E_x = 42.7$, $(P/h)/E_x = 0.003$, $R/h = 80$)

selection on contact length is that employing a stiffer material in the loading direction leads to a reduction in contact length. This outcome arises because a harder surface induces less indentation by the punch. Among the materials analyzed, B/Al demonstrates the highest stiffness in the loading direction, and the smallest contact length also occurs when this material is used. In comparing the analytical method with numerical techniques (FEM and ANN), the maximum relative errors are calculated as $e_{MAE(FEM)} = 2.15\%$ and $e_{MAE(ANN)} = 1.89\%$, while the average relative errors are $e_{MAE(FEM)} = 1.73\%$ and $e_{MAE(ANN)} = 1.49\%$, respectively.

Figure 12 presents the maximum contact stress at the interface between the punch and the orthotropic layer for various orthotropic materials. As can be seen from the figure, the stiffer the material in the loading direction, the higher the resulting maximum stress levels at the contact surface. When comparing the analytical solution with numerical methods (FEM and ANN), the maximum and average relative errors are found to be $e_{MAE(FEM)} = 2.48\%$, $e_{MAE(ANN)} = 1.89\%$, and $e_{MAE(FEM)} = 2.10$, $e_{MAE(ANN)} = 1.55\%$, respectively.

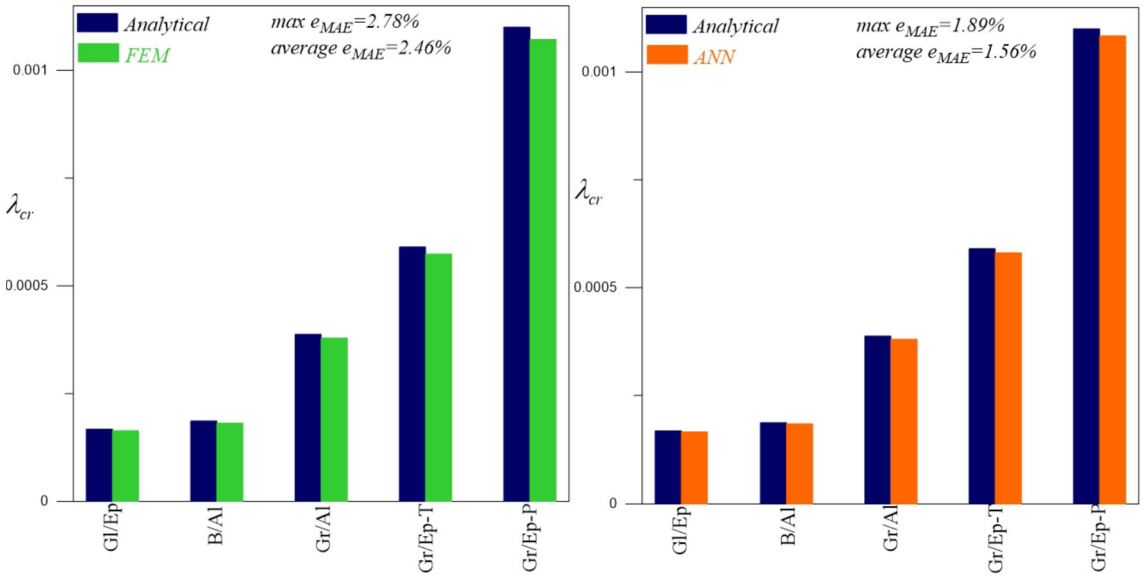


**Fig. 13** Effect of using different orthotropic materials on the critical separation load ($\rho gh/E_x = 10^{-6}$, $E_2/E_x = 1$, $\kappa_2 = 2$, $E_x = 144.8$, $(P/h)/E_x = 0.002$, $R/h = 100$)

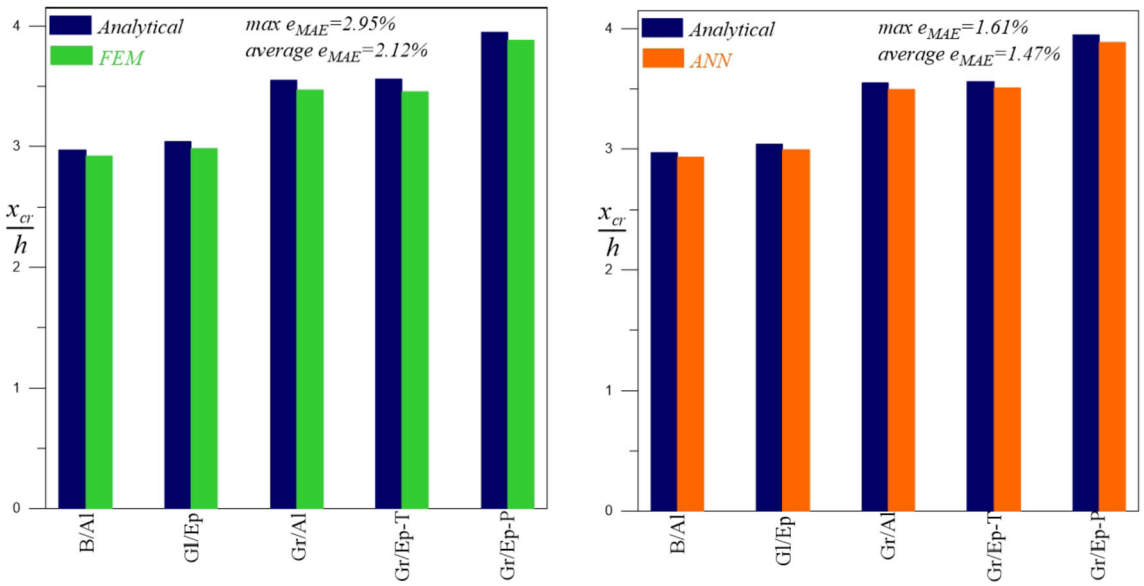


**Fig. 14** Effect of using different orthotropic materials on the critical separation distance ($\rho gh/E_x = 10^{-6}$, $E_2/E_x = 1$, $\kappa_2 = 2$, $E_x = 144.8$, $(P/h)/E_x = 0.002$, $R/h = 100$)

Figure 13 illustrates how the type of orthotropic material influences the critical load at which initial separation occurs between the orthotropic layer and the isotropic half-space. When the figure is examined, the smallest value of the critical load value required to separate the orthotropic layer from the isotropic half-space occurs in the case of using Gl/Ep material, while the largest value occurs in the case of using Gr/Ep-P material. The comparison between the analytical approach and numerical methods (FEM and ANN) yields maximum relative errors of $e_{MAE(FEM)} = 2.78\%$ and $e_{MAE(ANN)} = 1.89\%$, while the average relative errors are $e_{MAE(FEM)} = 2.46\%$ and $e_{MAE(ANN)} = 1.56\%$, respectively.

Figure 14 depicts the effect of using different orthotropic materials on the critical separation distance between the orthotropic layer and the isotropic half-space. When the figure is analyzed, the critical separation point between the orthotropic layer and the isotropic half-space occurs at the farthest point from the symmetry axis in the case of Gr/Ep-P material. When comparing the analytical approach to numerical methods (FEM

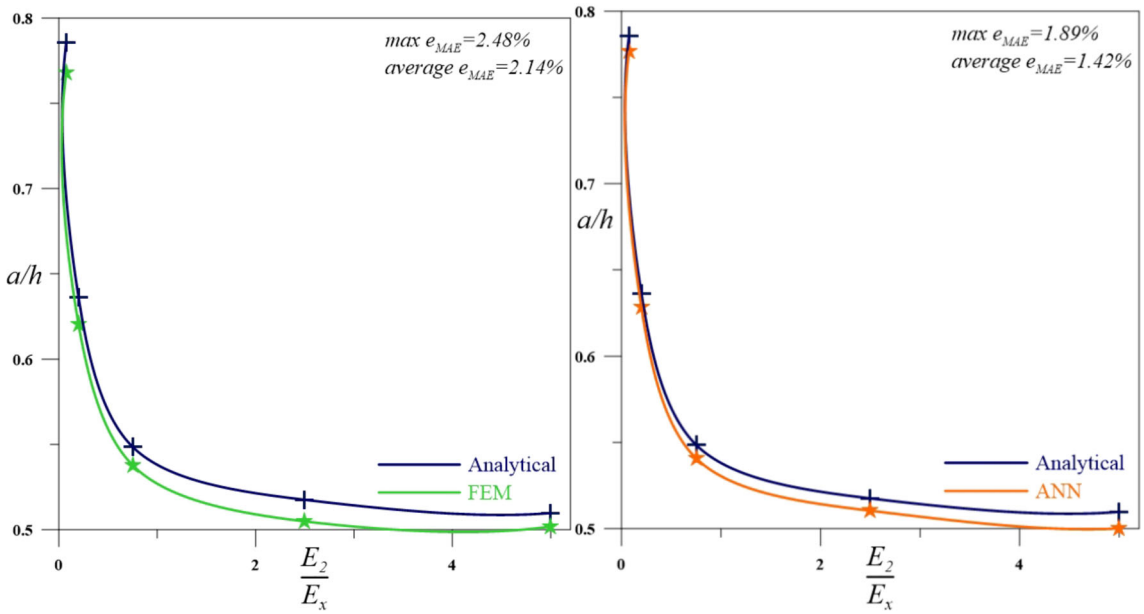


**Fig. 15** Variation of contact length with changing elastic modulus of the isotropic half-space ($\kappa_2 = 2$, R/h = 50, (P/h)/$E_x = 0.005$, B/Al)

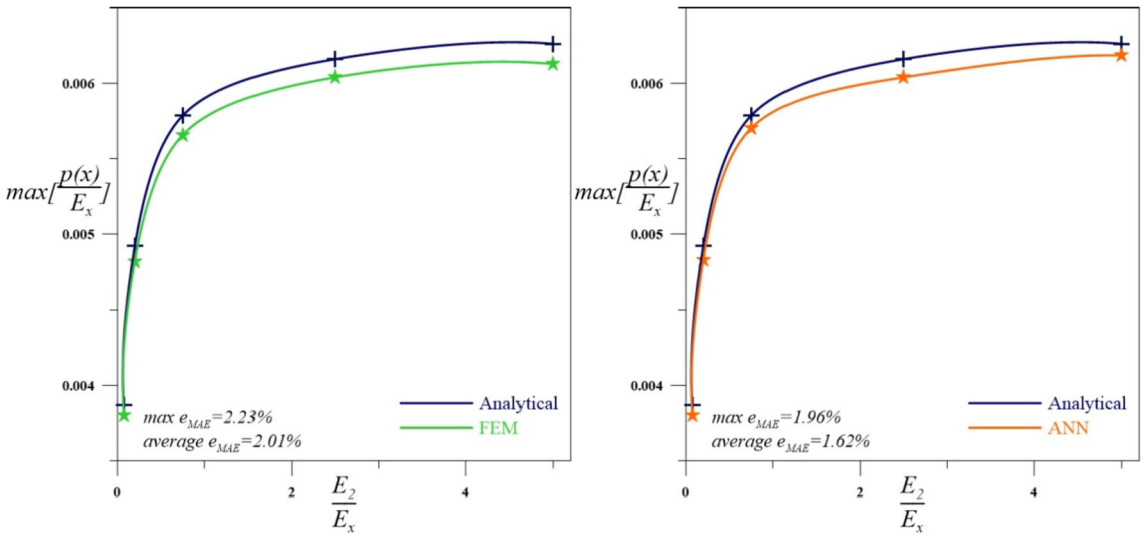


**Fig. 16** Variation of maximum contact stress with changing elastic modulus of the isotropic half-space ($\kappa_2 = 2$, R/h = 50, (P/h)/$E_x$ = 0.005, B/Al)

and ANN), the maximum relative errors for critical separation distance are found to be $e_{MAE(FEM)} = 2.95\%$ and $e_{MAE(ANN)} = 1.61\%$, with average relative errors of $e_{MAE(FEM)} = 2.12\%$ and $e_{MAE(ANN)} = 1.47\%$.

Figure 15 illustrates the effect of the dimensionless elastic modulus of the isotropic half-space on the contact length at the interface between the punch and the orthotropic layer. The figure demonstrates that an increase in the $E_2/E_x$ ratio, which indicates greater rigidity of the isotropic half-space, leads to a reduction in contact length. When comparing the analytical method with numerical approaches (FEM and ANN), the maximum and average relative errors in contact length are observed as $e_{MAE(FEM)} = 2.48\%$ and $e_{MAE(ANN)} = 1.89\%$, and $e_{MAE(FEM)} = 2.14\%$ and $e_{MAE(ANN)} = 1.42\%$, respectively.

Figure 16 shows how the dimensionless elastic modulus of the isotropic half-space affects the maximum contact stress at the interface between the punch and the orthotropic layer. The figure reveals that an increase in the $E_2/E_x$ ratio, which signifies greater rigidity of the isotropic half-space, results in higher maximum contact

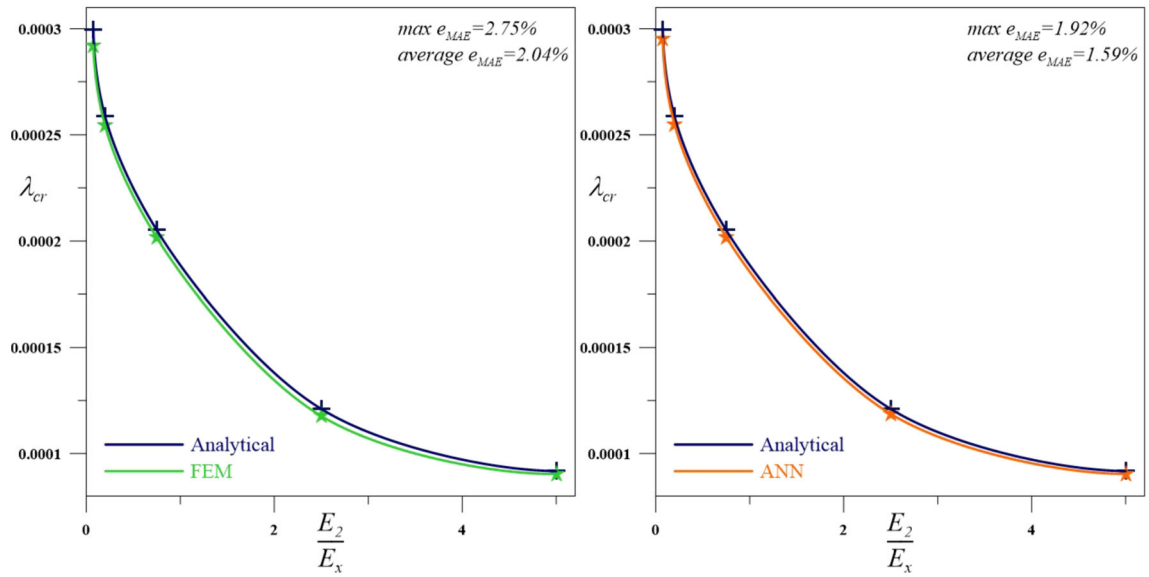


**Fig. 17** Variation of critical separation load with changing elastic modulus of the isotropic half-space ($\rho gh/E_x = 10^{-6}$, $\kappa_2 = 2$, $R/h = 50$, $(P/h)/E_x = 0.005$, B/Al)

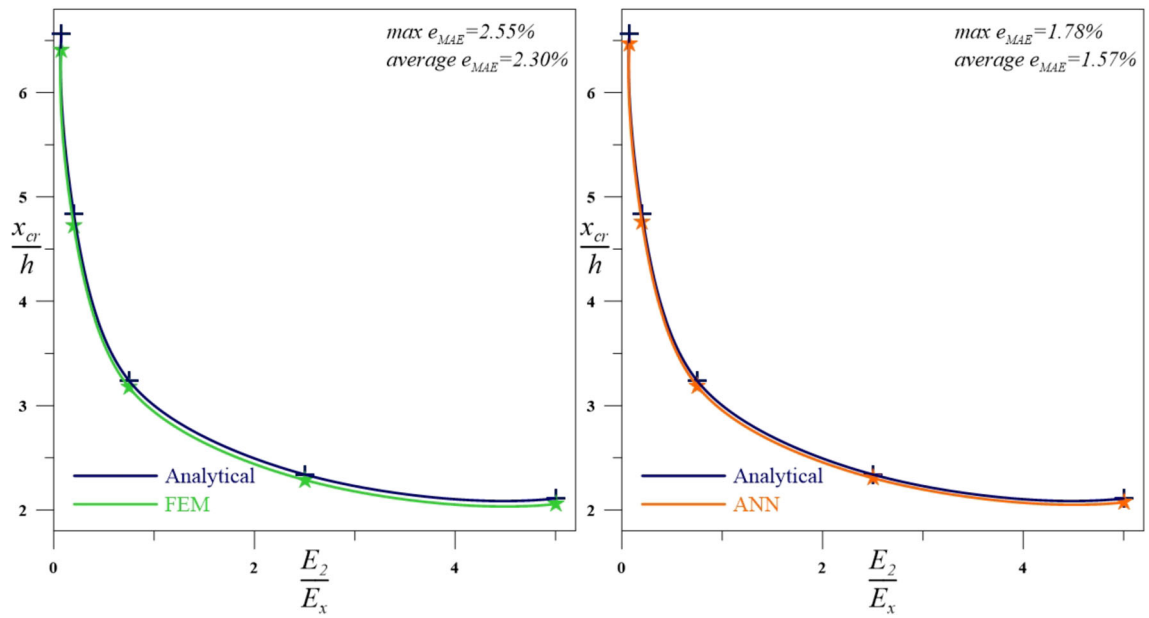


**Fig. 18** Variation of critical separation distance with changing elastic modulus of the isotropic half-space ($\rho gh/E_x = 10^{-6}$, $\kappa_2 = 2$, $R/h = 50$, $(P/h)/E_x = 0.005$, B/Al)

stresses. In comparing the analytical method with numerical techniques (FEM and ANN), the maximum and average relative errors in maximum contact stress are calculated as $e_{MAE(FEM)} = 2.23\%$ and $e_{MAE(ANN)} = 1.96\%$, and $e_{MAE(FEM)} = 2.01\%$ and $e_{MAE(ANN)} = 1.62\%$, respectively.

Figure 17 depicts the effect of the dimensionless elastic modulus of the isotropic half-space on the critical load required to initial separation between the orthotropic layer and the isotropic half-space. The results indicate that an increase in the $E_2/E_x$ ratio, which reflects a higher rigidity of the isotropic half-space, results in a lower critical load needed for initial separation. The analysis shows that the maximum and average relative errors are $e_{MAE(FEM)} = 2.75\%$ and $e_{MAE(ANN)} = 1.92\%$, and $e_{MAE(FEM)} = 2.04\%$ and $e_{MAE(ANN)} = 1.59\%$, respectively.

Figure 18 highlights the influence of the dimensionless elastic modulus of the isotropic half-space on the critical separation distance between the orthotropic layer and the isotropic half-space. The figure demonstrates

that an increase in the $E_2/E_x$ ratio, indicating greater rigidity of the isotropic half-space, results in a decrease in the distance at which the initial separation occurs, thereby moving this point closer to the axis of symmetry. The analysis comparing the analytical method with numerical approaches (FEM and ANN) reveals maximum relative errors of $e_{MAE(FEM)} = 2.55\%$ and $e_{MAE(ANN)} = 1.78\%$, and average relative errors of $e_{MAE(FEM)} = 2.30\%$ and $e_{MAE(ANN)} = 1.57\%$, respectively.

## 6 Conclusions

This study conducts a thorough investigation into the contact mechanics problem involving a homogeneous orthotropic layer and a homogeneous isotropic half-space, which are subjected to loading through a rigid cylindrical punch, employing three distinct approaches: analytical methods, the Finite Element Method (FEM), and Artificial Neural Network (ANN). The analytical solutions derived from elasticity theory are compared with results obtained from FEM and ANN.

The results reveal that the contact length, maximum contact stress, critical separation load, and critical separation distance are significantly influenced by various factors, including the punch radius, applied load, body forces, and material properties. Specifically, an increase in the punch radius leads to a larger contact length and a decrease in maximum contact stress, as expected. The analysis shows that a higher applied load results in increased contact length and maximum stress. Moreover, the type of orthotropic material and its stiffness in the loading direction notably affect the contact parameters. Stiffer orthotropic material in the loading direction leads to shorter contact lengths and higher maximum contact stresses.

The study reveals that as the $E_2/E_x$ ratio increases, indicating greater rigidity of the isotropic half-space, the contact length decreases, the maximum contact stresses increases, the critical load for initial separation reduces, and the critical separation distance becomes smaller. These findings highlight the sensitivity of the contact mechanics problem to changes in material properties and loading conditions. The comparative analysis demonstrates that both FEM and ANN methods provide highly accurate results, consistent with the analytical solutions, validating their effectiveness in addressing complex contact problems.

Overall, this study enhances the understanding of contact interactions between orthotropic and isotropic materials by integrating analytical and numerical approaches. The research fills a crucial gap in the literature by providing a detailed examination of how material, geometric properties and loading conditions influence contact mechanics.

**Author contributions** E.Ö. and M.G.O. conducted the analytical analysis and wrote the main manuscript text. E.U.Y. carried out the ANN analysis. M.Y. and I.M. performed the finite element analysis and prepared all figures and tables. All authors reviewed the manuscript.

**Funding** Open access funding provided by the Scientific and Technological Research Council of Türkiye (TÜBİTAK). No funding was received for conducting this study.

**Data availability** No datasets were generated or analysed during the current study.

### Declarations

**Conflict of interest** The authors declare no competing interests.

**Ethical approval** The authors declare that the research was conducted according to ethical standards.

**Open Access** This article is licensed under a Creative Commons Attribution 4.0 International License, which permits use, sharing, adaptation, distribution and reproduction in any medium or format, as long as you give appropriate credit to the original author(s) and the source, provide a link to the Creative Commons licence, and indicate if changes were made. The images or other third party material in this article are included in the article's Creative Commons licence, unless indicated otherwise in a credit line to the material. If material is not included in the article's Creative Commons licence and your intended use is not permitted by statutory regulation or exceeds the permitted use, you will need to obtain permission directly from the copyright holder. To view a copy of this licence, visit http://creativecommons.org/licenses/by/4.0/.

## Appendix

$$C_{11} = \frac{(1 - \nu_{yz}\nu_{zy})E_x}{\Delta_C} \tag{61}$$

$$C_{13} = \frac{(\nu_{zx} + \nu_{yx}\nu_{zy})E_x}{\Delta_C} \tag{62}$$

$$C_{33} = \frac{(1 - \nu_{xy}\nu_{yx})E_z}{\Delta_C} \tag{63}$$

$$C_{55} = \mu_{xz} \tag{64}$$

$$\Delta_C = 1 - \nu_{xy}\nu_{yx} - \nu_{yz}\nu_{zy} - \nu_{xz}\nu_{zx} - 2\nu_{xz}\nu_{yx}\nu_{zy} \tag{65}$$

$$\Gamma(x,t) = \int_0^\infty \frac{\Gamma_1(\alpha) - \Lambda}{\Lambda} \sin\alpha(t-x)d\alpha \tag{66}$$

$$\Gamma_1(\alpha) = \sum_{i=1}^{4} -\alpha A_i^K \mho_i e^{\eta_i \alpha h} \tag{67}$$

$$\Lambda = \lim_{\alpha\to\infty} \Gamma_1(\alpha) \tag{68}$$

$$\zeta(x,t) = \int_0^\infty \zeta_1(\alpha,0)\mathrm{Cos}[\alpha(t-x)]d\alpha \tag{69}$$

$$\zeta_1(\alpha,0) = \alpha \sum_{i=1}^{4} A_i^K (C_{13} + C_{33}\mho_i\eta_i) \tag{70}$$

## References


1. Lim, T.-C.: Contact and indentation mechanics of auxetic materials. In: Lim, T.-C. (ed.) Auxetic materials and structures, pp. 171–199. Springer, Singapore (2015)
2. Chenxi, Z., Shenghu, D.: Continuous contact problem of thermoelectric layer pressed by rigid punch. Appl. Math. Model. **100**, 536–548 (2021). https://doi.org/10.1016/j.apm.2021.07.029
3. Cwiekala, N., Barber, J.R., Hills, D.A.: Memory-free loading paths for a coupled continuous contact problem with friction. Mech. Res. Commun. **124**, 103958 (2022). https://doi.org/10.1016/j.mechrescom.2022.103958
4. Öner, E., Adıyaman, G., Birinci, A.: Continuous contact problem of a functionally graded layer resting on an elastic half-plane. Arch. Mech. **69**, 53–73 (2017)
5. Öner, E., Birinci, A.: Continuous contact problem for two elastic layers resting on an elastic half-infinite plane. J. Mech. Mater. Struct. **9**, 105–119 (2014). https://doi.org/10.2140/jomms.2014.9.105
6. Polat, A., Kaya, Y., Özşahin, T.Ş: Analytical solution to continuous contact problem for a functionally graded layer loaded through two dissimilar rigid punches. Meccanica **53**, 3565–3577 (2018). https://doi.org/10.1007/s11012-018-0902-7
7. Zhang, C., Zhang, B., Zhou, Y., Ding, S.: Continuous contact problem of interaction between two arbitrarily positioned flat stamps on the thermoelectric material. Acta Mech. **234**, 4719–4732 (2023). https://doi.org/10.1007/s00707-023-03610-6
8. Oner, E., Yaylaci, M., Birinci, A.: Analytical solution of a contact problem and comparison with the results from FEM. Struct. Eng. Mech. **54**, 607–622 (2015). https://doi.org/10.12989/sem.2015.54.4.607
9. Adıyaman, G., Öner, E., Birinci, A.: Continuous and discontinuous contact problem of a functionally graded layer resting on a rigid foundation. Acta Mech. **228**, 3003–3017 (2017). https://doi.org/10.1007/s00707-017-1871-y
10. Öner, E., Birinci, A.: Investigation of the solution for discontinuous contact problem between a functionally graded (FG) layer and homogeneous half-space. Arch. Appl. Mech. **90**, 2799–2819 (2020). https://doi.org/10.1007/s00419-020-01750-y
11. Shvets, R.M., Martynyak, R.M., Kryshtafovych, A.A.: Discontinuous contact of an anisotropic half-plane and a rigid base with disturbed surface. Int. J. Eng. Sci. **34**, 183–200 (1996). https://doi.org/10.1016/0020-7225(95)00091-7
12. Zhang, C., Ding, S.: Frictionless discontinuous contact problem of the thermoelectric layer resting on a rigid base. J. Therm. Stress. **45**, 817–831 (2022). https://doi.org/10.1080/01495739.2022.2104768
13. Ahn, Y.J., Barber, J.R.: Response of frictional receding contact problems to cyclic loading. Int. J. Mech. Sci. **50**, 1519–1525 (2008). https://doi.org/10.1016/j.ijmecsci.2008.08.003
14. El-Borgi, S., Abdelmoula, R., Keer, L.: A receding contact plane problem between a functionally graded layer and a homogeneous substrate. Int. J. Solids Struct. **43**, 658–674 (2006). https://doi.org/10.1016/j.ijsolstr.2005.04.017
15. Lopes, J.P., Hills, D.A.: The axisymmetric frictional receding contact of a layer pressed against a half-space by a point force. Int. J. Solids Struct. **171**, 47–53 (2019). https://doi.org/10.1016/j.ijsolstr.2019.05.007

16. Öner, E., Şengül Şabano, B., Uzun Yaylacı, E., Adıyaman, G., Yaylacı, M., Birinci, A.: On the plane receding contact between two functionally graded layers using computational, finite element and artificial neural network methods. J. Appl. Math. Mech. **102**, e202100287 (2022). https://doi.org/10.1002/zamm.202100287
17. Öner, E., Yaylacı, M., Birinci, A.: Solution of a receding contact problem using an analytical method and a finite element method. J. Mech. Mater. Struct. **9**, 333–345 (2014). https://doi.org/10.2140/jomms.2014.9.333
18. Rhimi, M., El-Borgi, S., Lajnef, N.: A double receding contact axisymmetric problem between a functionally graded layer and a homogeneous substrate. Mech. Mater. **43**, 787–798 (2011). https://doi.org/10.1016/j.mechmat.2011.08.013
19. Ting-Ting Wang, Y.-R.L., Huang, G.-Y.: Effect of adhesion on the frictionless receding contact between an elastic layer and a substrate. J. Adhes. **100**, 63–81 (2024). https://doi.org/10.1080/00218464.2023.2194534
20. Wang, C., Yan, J., Cao, R.: On the receding contact plane problem for bi-FGM-layers indented by a flat indenter. Struct. Eng. Mech. **85**, 621–633 (2023)
21. Yan, J., Li, X.: Double receding contact plane problem between a functionally graded layer and an elastic layer. Eur. J. Mech. A. Solids **53**, 143–150 (2015). https://doi.org/10.1016/j.euromechsol.2015.04.001
22. Adıyaman, G., Birinci, A., Öner, E., Yaylacı, M.: A receding contact problem between a functionally graded layer and two homogeneous quarter planes. Acta Mech. **227**, 1753–1766 (2016). https://doi.org/10.1007/s00707-016-1580-y
23. Aleksandrov, V.M., Kostyreva, L.A.: The plane contact problem for a prestressed incompressible elastic layer. J. Appl. Math. Mech. **73**, 705–709 (2009). https://doi.org/10.1016/j.jappmathmech.2010.02.001
24. Czekanski, A., Zozulya, V.V.: Comparative study of time and frequency domain approaches in contact problem for the I-mode crack under harmonic loading. Eng. Anal. Bound. Elem. **95**, 200–214 (2018). https://doi.org/10.1016/j.enganabound.2018.07.009
25. Sofonea, M., Matei, A.: Elastic antiplane contact problem with adhesion. Z. Für Angew. Math. Phys. **53**, 962–972 (2002). https://doi.org/10.1007/PL00012622
26. Vodička, R., Mantič, V., Roubíček, T.: Quasistatic normal-compliance contact problem of visco-elastic bodies with Coulomb friction implemented by QP and SGBEM. J. Comput. Appl. Math. **315**, 249–272 (2017). https://doi.org/10.1016/j.cam.2016.10.010
27. Yaylacı, A., Öner, B.: Examination of analytical and finite element solutions regarding contact of a functionally graded layer. Struct. Eng. Mech. **76**, 325–336 (2020). https://doi.org/10.12989/sem.2020.76.3.325
28. Gao, X.-L., Mao, C.L.: Solution of the contact problem of a rigid conical frustum indenting a transversely isotropic elastic half-space. J. Appl. Mech. (2013). https://doi.org/10.1115/1.4025140
29. Fabrikant, V.I.: Contact problem for a transversely isotropic half-space limited by a plane perpendicular to its planes of isotropy. IMA J. Appl. Math. **81**, 199–227 (2016). https://doi.org/10.1093/imamat/hxv032
30. Wu, F., Li, C.: Partial slip contact problem between a transversely isotropic half-space of multi-ferroic composite medium and a spherical indenter. Mech. Mater. **161**, 104018 (2021). https://doi.org/10.1016/j.mechmat.2021.104018
31. Doblare, M., Espiga, F., Gracia, L., Alcantud, M.: Contact tractions between orthotropic materials by using the boundary element method. Eng. Anal. Bound. Elem. **9**, 125–136 (1992). https://doi.org/10.1016/0955-7997(92)90053-A
32. Zhang, H.W., He, S.Y., Li, X.S., Wriggers, P.: A new algorithm for numerical solution of 3D elastoplastic contact problems with orthotropic friction law. Comput. Mech. (2004). https://doi.org/10.1007/s00466-004-0548-2
33. Pedersen, P.: On the influence of clearance in orthotropic disc-pin contacts. Compos. Struct. **79**, 554–561 (2007). https://doi.org/10.1016/j.compstruct.2006.02.029
34. Guler, M.A.: Closed-form solution of the two-dimensional sliding frictional contact problem for an orthotropic medium. Int. J. Mech. Sci. **87**, 72–88 (2014). https://doi.org/10.1016/j.ijmecsci.2014.05.033
35. Arslan, O., Dag, S.: Contact mechanics problem between an orthotropic graded coating and a rigid punch of an arbitrary profile. Int. J. Mech. Sci. **135**, 541–554 (2018). https://doi.org/10.1016/j.ijmecsci.2017.12.017
36. Öner, E.: Two-dimensional frictionless contact analysis of an orthotropic layer under gravity. J. Mech. Mater. Struct. **16**, 573–594 (2021). https://doi.org/10.2140/jomms.2021.16.573
37. Oner, E.: Frictionless contact mechanics of an orthotropic coating/isotropic substrate system. Comput. Concr. **28**, 209–220 (2021)
38. Yang, L., Guo, C., Cao, D., Han, Z., Wang, F.: Analysis of dynamic response of two-dimensional orthotropic layered media with imperfect interfaces between layers. Appl. Math. Model. **101**, 171–194 (2022). https://doi.org/10.1016/j.apm.2021.07.033
39. Öner, E.: Computational contact mechanics for a medium consisting of functionally graded material coating and orthotropic substrate. J. Struct. Eng. Appl. Mech. **4**, 249–266 (2021). https://doi.org/10.31462/jseam.2021.04249266
40. Urquhart, E.E., Pindera, M.-J.: Incipient separation between a frictionless flat punch and an anisotropic multilayered half plane. Int. J. Solids Struct. **31**, 2445–2461 (1994). https://doi.org/10.1016/0020-7683(94)90030-2
41. Çömez, İ: Frictional moving contact problem between a functionally graded monoclinic layer and a rigid punch of an arbitrary profile. Acta Mech. **233**, 1435–1453 (2022). https://doi.org/10.1007/s00707-022-03178-7
42. Song, H.-X., Ke, L.-L., Su, J., Yang, J., Kitipornchai, S., Wang, Y.-S.: Surface effect on the contact problem of a piezoelectric half-plane. Int. J. Solids Struct. **185–186**, 380–393 (2020). https://doi.org/10.1016/j.ijsolstr.2019.07.024
43. Lv, X., Ke, L.-L., Su, J., Tian, J.-Y.: Axisymmetric contact vibration analysis of a rigid spherical punch on a piezoelectric half-space. Int. J. Solids Struct. **210–211**, 224–236 (2021). https://doi.org/10.1016/j.ijsolstr.2020.11.029
44. Bouchantouf, R., Baiz, O., Moutawakil, D.E., Benaissa, H.: Optimal control of a frictional thermo-piezoelectric contact problem. Int. J. Dyn. Control. **11**, 821–834 (2023). https://doi.org/10.1007/s40435-022-01019-y
45. Alaoui, M., Essoufi, E.-H., Ouaanabi, A., Bouallala, M.: On the dynamic Coulomb's frictional contact problem for thermo-piezoelectric materials. J. Appl. Math. Mech. **104**, 1202300891 (2024). https://doi.org/10.1002/zamm.202300891
46. Parel, K.S.: Contact mechanics of a thin layer pressed onto a substrate by a line load. J. Appl. Mech. (2020). https://doi.org/10.1115/1.4045717
47. Chen, X.W., Yue, Z.Q.: Incomplete contact between a coated elastic substrate and rigid foundation perturbed by a rigid disc. Int. J. Solids Struct. **202**, 605–619 (2020). https://doi.org/10.1016/j.ijsolstr.2020.06.017

48. Adıyaman, G., Öner, E., Yaylacı, M., Birinci, A.: A study on the contact problem of a layer consisting of functionally graded material (FGM) in the presence of body force. J. Mech. Mater. Struct. **18**, 125–141 (2023). https://doi.org/10.2140/jomms.2023.18.125
49. Zhang, R., Zhao, G., Wang, W., Du, X.: Large deformation frictional contact formulations for isogeometric Kirchhoff-Love shell. Int. J. Mech. Sci. **249**, 108253 (2023). https://doi.org/10.1016/j.ijmecsci.2023.108253
50. Yaylacı, M., Öner, E., Adıyaman, G., Öztürk, Ş, Uzun Yaylacı, E., Birinci, A.: Analyzing of continuous and discontinuous contact problems of a functionally graded layer: theory of elasticity and finite element method. Mech. Based Des. Struct. Mach. **52**, 5720 (2023)
51. Zhang, Y., Zhou, Y., Ding, S.: Frictional contact analysis of a rigid solid with periodic surface sliding on the thermoelectric material. Appl. Math. Mech. **45**, 179–196 (2024). https://doi.org/10.1007/s10483-024-3075-7
52. Hilding, D.: The equilibrium state of a structure subject to frictional contact. Eur. J. Mech. A. Solids **19**, 1029–1040 (2000). https://doi.org/10.1016/S0997-7538(00)00203-5
53. Hassani, R., Hild, P., Ionescu, I.R., Sakki, N.-D.: A mixed finite element method and solution multiplicity for Coulomb frictional contact. Comput. Methods Appl. Mech. Eng. **192**, 4517–4531 (2003). https://doi.org/10.1016/S0045-7825(03)00419-5
54. Zhang, X., Kneupner, K., Kuhlenkötter, B.: A new force distribution calculation model for high-quality production processes. Int. J. Adv. Manuf. Technol. **27**, 726–732 (2006). https://doi.org/10.1007/s00170-004-2229-x
55. Campo, M., Fernández, J.R., Kuttler, K.L.: Analysis of a dynamic frictional contact problem with damage. Finite Elem. Anal. Des. **45**, 659–674 (2009). https://doi.org/10.1016/j.finel.2009.05.001
56. Birinci, A., Adıyaman, G., Yaylacı, M., Öner, E.: Analysis of continuous and discontinuous cases of a contact problem using analytical method and FEM. Lat. Am. J. Solids Struct. **12**, 1771–1789 (2015)
57. Yue, J., Liu, G.-R., Li, M., Niu, R.: A cell-based smoothed finite element method for multi-body contact analysis using linear complementarity formulation. Int. J. Solids Struct. **141–142**, 110–126 (2018). https://doi.org/10.1016/j.ijsolstr.2018.02.016
58. Bonari, J., Marulli, M.R., Hagmeyer, N., Mayr, M., Popp, A., Paggi, M.: A multi-scale FEM-BEM formulation for contact mechanics between rough surfaces. Comput. Mech. **65**, 731–749 (2020). https://doi.org/10.1007/s00466-019-01791-3
59. Yaylaci, M., Adiyaman, G., Oner, E., Birinci, A.: Investigation of continuous and discontinuous contact cases in the contact mechanics of graded materials using analytical method and FEM. Comput. Concr. **27**, 199–210 (2021)
60. Sui, Y., Wang, W., Zhang, H.: Effects of electromagnetic fields on the contact of magneto-electro-elastic materials. Int. J. Mech. Sci. **223**, 107283 (2022). https://doi.org/10.1016/j.ijmecsci.2022.107283
61. Öner, E., Uzun Yaylacı, E., Yaylacı, M.: Multi-method examination of contact mechanics in orthotropic layers under gravity. Mech. Mater. **195**, 105036 (2024). https://doi.org/10.1016/j.mechmat.2024.105036
62. Yaylacı, M., Öner, E., Birinci, A.: Comparison between analytical and ANSYS calculations for a receding contact problem. J. Eng. Mech. **140**, 04014070 (2014)
63. Zhao, X., Li, Z.: The solution of frictional wheel–rail rolling contact with a 3D transient finite element model: validation and error analysis. Wear **271**, 444–452 (2011). https://doi.org/10.1016/j.wear.2010.10.007
64. Machado, M., Moreira, P., Flores, P., Lankarani, H.M.: Compliant contact force models in multibody dynamics: evolution of the Hertz contact theory. Mech. Mach. Theory **53**, 99–121 (2012). https://doi.org/10.1016/j.mechmachtheory.2012.02.010
65. Zhou, K., Wei, R.: Modeling cracks and inclusions near surfaces under contact loading. Int. J. Mech. Sci. **83**, 163–171 (2014). https://doi.org/10.1016/j.ijmecsci.2014.03.028
66. Güler, M.A., Kucuksucu, A., Yilmaz, K.B., Yildirim, B.: On the analytical and finite element solution of plane contact problem of a rigid cylindrical punch sliding over a functionally graded orthotropic medium. Int. J. Mech. Sci. **120**, 12–29 (2017). https://doi.org/10.1016/j.ijmecsci.2016.11.004
67. Yaylacı, M., Eyüboğlu, A., Adıyaman, G., Yaylacı, E.U., Öner, E., Birinci, A.: Assessment of different solution methods for receding contact problems in functionally graded layered mediums. Mech. Mater. **154**, 103730 (2021). https://doi.org/10.1016/j.mechmat.2020.103730
68. Li, Y.-H., Shen, F., Güler, M.A., Ke, L.-L.: Modeling multi-physics electrical contact on rough surfaces considering elastic-plastic deformation. Int. J. Mech. Sci. **269**, 109066 (2024). https://doi.org/10.1016/j.ijmecsci.2024.109066
69. Karabulut, P.M., Çetinkaya, İT., Oğuz, H., Çömez, İ: Moving contact problem of a functionally graded orthotropic coated half plane. Acta Mech. **235**, 3989–4004 (2024). https://doi.org/10.1007/s00707-024-03927-w
70. Öner, E., Al-Qado, A.W.H.: Analytical approach to contact mechanics of functionally graded orthotropic layers with gravitational considerations. Acta Mech. **235**, 6929–6958 (2024). https://doi.org/10.1007/s00707-024-04091-x
71. Öner, E., Al-Qado, A.W.H.: Contact mechanics of functionally graded orthotropic layer under normal traction and gravity: an analytical perspective. Arch. Appl. Mech. **95**, 23 (2025). https://doi.org/10.1007/s00419-024-02733-z
72. Li, P., Liu, T.-J., He, R.: Sliding friction contact problem from the perspective of the micropolar elasticity theory. Acta Mech. Sin. **41**, 424417 (2025). https://doi.org/10.1007/s10409-024-24417-x
73. Radi, E., Falope, F.O., Lanzoni, L.: Advancing contact between a rigid pin and a FGM circular beam with clearance. Int. J. Solids Struct. **311**, 113244 (2025). https://doi.org/10.1016/j.ijsolstr.2025.113244
74. Öner, E., Oktay, M.G.: Semi-analytical analysis of orthotropic-isotropic contact in layered media with consideration of body forces. J. Braz. Soc. Mech. Sci. Eng. **47**, 63 (2025). https://doi.org/10.1007/s40430-024-05374-z
75. Zhang, Y., Zhou, Y., Yang, W., Wang, W., Ding, S.: Periodic partial slip contact of thermoelectric materials under flat punches or cylindrical punches. Acta Mech. Sin. **41**, 424676 (2025). https://doi.org/10.1007/s10409-024-24676-x
76. Civelek, M.B., Erdogan, F.: The frictionless contact problem for an elastic layer under gravity. J. Appl. Mech. **42**, 136–140 (1975). https://doi.org/10.1115/1.3423504
77. Erdogan, F., Gupta, G.: On the numerical solution of singular integral equations. Q. Appl. Math. **29**, 525–534 (1972)
78. Yaylaci, E.U., Özdemir, M.E., Güvercin, Y., Öztürk, Ş, Yaylaci, M.: Analysis of the mechano-bactericidal effects of nanopatterned surfaces on implant-derived bacteria using the FEM. Adv. Nano Res. **15**, 567–577 (2023)
79. Adiyaman, G., Oner, E., Yaylaci, M., Birinci, A.: The contact problem of a functionally graded layer under the effect of gravity. J. Appl. Math. Mech. **103**, e202200560 (2023). https://doi.org/10.1002/zamm.202200560

80. Yaylacı, E.U., Öner, E., Yaylacı, M., Özdemir, M.E., Abushattal, A., Birinci, A.: Application of artificial neural networks in the analysis of the continuous contact problem. Struct. Eng. Mech. Intl J. **84**, 35–48 (2022)
81. ANSYS Contact Technology Guide. Ansys Inc, Canonsbur (2013)
82. Binienda, W.K., Pindera, M.-J.: Frictionless contact of layered metal-matrix and polymer-matrix composite half planes. Compos. Sci. Technol. **50**, 119–128 (1994). https://doi.org/10.1016/0266-3538(94)90131-7

**Publisher's Note** Springer Nature remains neutral with regard to jurisdictional claims in published maps and institutional affiliations.